UPPSALA
UNIVERSITET

ZrN Back-Contact Reflectors and Ga Gradients in Cu(In,Ga)Se$_2$ Solar Cells

SEBASTIAN MICHAEL SCHLEUSSNER

Abstract

Solar cells constitute the most direct way of converting solar energy to electricity, and thin-film solar-cell technologies have lately been growing in importance, allowing the fabrication of less expensive modules that nonetheless have good power-conversion efficiencies. This thesis focuses on solar cells based on Cu(In,Ga)Se$_2$, which is the thin-film technology that has shown the highest conversion efficiency to date, reaching 20.3 % on the laboratory scale. Solar modules still have some way to go to become entirely competitive with existing energy technologies, and there are two possible paths to this goal: Firstly, reducing their manufacturing costs, for instance by minimizing the material usage per module and/or by increasing the throughput of a given factory; and secondly, increasing the power output per module in other words, the module efficiency. The subject matters of this thesis are related to those two approaches.

The first issue investigated is the possibility for reducing the thickness of the Cu(In,Ga)Se$_2$ layer and compensating for lost absorption by using a ZrN back reflector. ZrN layers are fabricated by reactive sputtering and I present a method for tuning the sputtering parameters so as to obtain a back reflector with good optical, electrical and mechanical properties. The reflector layer cannot be used directly in CIGS devices, but relatively good devices can be achieved with a precursor providing a homogeneous supply of Na, the addition of a very thin sacrificial Mo layer that allows the formation of a film of MoSe$_2$ passivating the back contact, and optionally a Ga gradient that further keeps electrons away from the back contact.

The second field of study concerns the three-stage CIGS coevaporation process, which is widely used in research labs around the world and has yielded small-area cells with highest efficiencies, but has not yet made it to large scale production. My focus lies on the development and the effect of gradients in the $[\text{Ga}]/[\text{In}+\text{Ga}]$ ratio. On the one hand, I investigate 'intrinsic' gradients (ones that form autonomously during the evaporation), and present a formation model based on the differing diffusivity of Ga and In atoms in CIGS and on the development along the quasi-binary tie line between $(\text{In,Ga})_2\text{Se}_3$ and Cu_2Se. On the other hand, I determine how the process should be designed in order to preserve 'extrinsic' gradients due to interdiffusion. Lastly, I examine the electrical effects of Ga-enhancement at the back and at the front of the absorber and of In-enhancement at the front. Over a wide range, In-rich top layers prove to have no or a weakly beneficial effect, while Ga-rich top regions pose a high risk to have a devastating effect on device performance.

Keywords: Solar cells, CIGS, ZrN, three-stage process, multi-stage process, grading, SIMS, electrical modelling

Sebastian Michael Schleussner, Department of Engineering Sciences, Solid State Electronics, Uppsala University, Box 534, SE–751 21 Uppsala, Sweden

"If a thing is worth doing, it is worth doing badly."

— *Gilbert Keith Chesterton*
What's Wrong With The World (1910)

"… at first."

— *The Reformed Perfectionist's Creed*

List of Papers

This thesis is based on the following papers, which are referred to in the text by their Roman numerals.

I   **"Enhanced back reflectance and quantum efficiency in Cu(In,Ga)Se$_2$ thin film solar cells with a ZrN back reflector"**, Jonas Malmström, Sebastian Schleussner and Lars Stolt (2004), *Applied Physics Letters* **85** (13) pp. 2634–2636, doi:10.1063/1.1794860.

II   **"Reactively sputtered ZrN for application as reflecting back contact in Cu(In,Ga)Se$_2$ solar cells"**, Sebastian Schleussner, Tomáš Kubart, Tobias Törndahl and Marika Edoff (2009), *Thin Solid Films* **517** pp. 5548–5552, doi:10.1016/j.tsf.2009.03.196.

III   **"Effect of gallium grading in Cu(In,Ga)Se$_2$ solar-cell absorbers produced by multi-stage coevaporation"**, Sebastian Schleussner, Uwe Zimmermann, Timo Wätjen, Klaus Leifer and Marika Edoff (2011), *Solar Energy Materials and Solar Cells* **95** (2) pp. 721–726, doi:10.1016/j.solmat.2010.10.011.

IV   **"Technological and economical aspects on the influence of reduced CIGS thickness and Ga grading for co-evaporated CIGS modules"**, Marika Edoff, Sebastian Schleussner, Erik Wallin and Olle Lundberg (2011), *Proceedings of the E-MRS, 2010*, *Thin Solid Films* (article in press), doi:10.1016/j.tsf.2011.01.369.

V   **"Surface engineering in CIGS solar cells"**, Sebastian Schleussner, Jonas Pettersson, Tobias Törndahl and Marika Edoff (2011), submitted to *Progress in Photovoltaics: Research and Applications*.

VI   **"Development of gallium gradients in multi-stage Cu(In,Ga)Se$_2$ co-evaporation processes"**, Sebastian Schleussner, Tobias Törndahl, Margareta Linnarsson, Uwe Zimmermann, Timo Wätjen and Marika Edoff (2011), *Progress in Photovoltaics: Research and Applications* (accepted for publication).

Further papers, not included in the thesis

   i "**Influence of the N_2 gas flow on optical and structural properties of reactively sputtered ZrN**", <u>Sebastian Schleussner</u>, Tobias Törndahl and Marika Edoff (2007), *Proceedings of the 17th International Vacuum Congress* (Stockholm), *Journal of Physics: Conference Series* **100** (8) pp. 082016 ff, doi:10.1088/1742-6596/100/8/082016.

  ii "**Potential of optical improvements of the back contact in thin Cu(In,Ga)Se$_2$ solar cells**", Andrej Čampa, Gregor Černivec, <u>Sebastian Schleussner</u>, Janez Krč, Marika Edoff and Marko Topič (2007), *Proceedings of the 22nd European Photovoltaic Solar Energy Conference* (Milano) 3CO.9.2, urn:nbn:se:uu:diva-12396.

 iii "**Highly productive manufacturing of CIS-based large-area modules**", Michael Powalla, Friedrich Kessler, . . . , <u>Sebastian Schleussner</u>, et al. (2007), *Proceedings of the 22nd European Photovoltaic Solar Energy Conference* (Milano) 3DO.9.2, urn:nbn:se:uu:diva-12897.

  iv "**Sputtering of highly adhesive Mo back contact layers for Cu(In,Ga)Se$_2$ solar cells**", Marika Edoff, Nicolas Viard, Timo Wätjen, <u>Sebastian Schleussner</u>, Per-Oskar Westin and Klaus Leifer (2009), *Proceedings of the 24th European Photovoltaic Solar Energy Conference* (Hamburg) pp. 3037 ff, urn:nbn:se:uu:diva-113931.

Contents

List of Tables

List of Figures

Preface

This document is the harvest of a long period of work that has seen diverse and far journeys of mine. There is the journey from *Diplomingenieur* towards a doctorate, naturally – which was the very idea of this endeavour. But in the shadow of that one, there were other journeys, too: that from electrical engineer to something of a materials researcher; from guest "doing in Rome as the Romans do" in a seemingly familiar 'sibling' culture to mine, to felt stranger in a strange land running into severe cases of intercultural misunderstanding, to expat with growing insights about both my home and host country; from scared perfectionist to dreadnought (well: almost!) realist (well: almost!) trying to live by the "Reformed Perfectionist's Creed" printed in the beginning of this book; and others more that I will not bore you with. Many deserve acknowledgement for their support and companionship on this way – more than I can possibly name individually, but I will at least make a start.

To begin with, many thanks to my boss and primary supervisor *Marika Edoff* for taking me on as a postgraduate student and unwaveringly supporting and believing in me even at the times when progress was faltering and we had difficulties making our concepts comprehensible to each other. Special thanks for the wonderful support in the last few weeks! Marika also again and again would spend much frustrated time and effort convincing more or less willing Swedish and European authorities[1] to support us so that our group stayed alive and thriving. All of that has been very much appreciated!

Thanks also to my second supervisor *Tobias Törndahl*, for his support with all kinds of valuable X-ray measurements and for much friendly encouragement and advice (not least cautioning against over-interpreting data!).

Uwe Zimmermann, who came on board as an official third supervisor some two years ago but was around from the get-go (unless when his time was being monopolized by a Company That Shall Not Be Named), deserves great thanks for countless instances of practical, scientific and moral support: Constructing the new electronic setup for the BAK, acting as a fire brigade in all sorts of lab troubles, discussing big and small questions about data interpretation or physical laws (usually helping me understand far more than what I had asked for!), . . . – the list could easily go on.

Hélène Jonzon at Länshälsan helped me greatly during a crucial phase in overcoming the hinders built up by perfectionism and miscommunication.

---

[1] Of these, the EU's project LARCIS should be acknowledged in particular for financing a major part of my research term.

1. Introduction

Proverb has it that "money makes the world go round", and that may be true in some respects. However, what really, fundamentally 'makes the world go round', what keeps our modern societies and economies working, is *energy*.

According to the International Energy Agency (IEA) [61], the world's final-energy[1] consumption in the year 2008 was 8428 Megatonnes of oil equivalent (Mtoe), or 100 PWh (100 million million kWh), of which 17.2 % were utilized in the form of electricity. Today, most of the total energy demand is still met by the fossil fuels oil, coal and natural gas, but the balance will have to change in the nearer future. That is not only because of the contribution of the named sources to climate change, but also because the fossil fuels are going to become increasingly hard and expensive to get at as the "lowest-hanging fruits" among the deposits are being depleted. For countries that do not have many fossil resources in their own ground, reducing their dependence on fuel imports is yet another incentive for looking for alternatives.

Contrast to this the fact the power density of sunlight reaching the surface of our planet on a sunny day is approximately $1000 \, \text{W}/\text{m}^2$. When you crunch the numbers[2], you find that the energy that reaches the sun-facing half sphere of the Earth in one minute corresponds to today's global energy consumption for three days! So there is indeed a huge supply of power available from the Sun, one that is free ("the sun sends no invoice", as one company's advert saying goes) and is not going to deplete for aeons to come.

The question, then, is how to tap this supply, and the general answer is given by the field of *renewable energies*, which includes wind, hydro and wave power, biomass, solar heat, solar-thermal power, and photovoltaics. They all have their strengths and their weaknesses: Biomass power plants, for instance, can be controlled to meet demand just like conventional power plants; but unless using organic rests, biomass competes for area with food plants, and the amount of energy that can be harvested in one year from a certain area is many times smaller than with photovoltaics.

---

[1] When talking about energy statistics, *primary energy* is used to mean the energy available in nature, for instance in coal, gas, wind or solar radiation. *Final energy* is then the energy actually utilized by "consumers", subtracting from primary energy the losses occurring in conversion (for instance in refineries or power plants), storage (e. g. by leaks in gas tanks) and transport (e. g. through power lines).

[2] With a diameter of about 12 700 km, Earth has a cross-sectional area of roughly 126 million square kilometres facing the sun at any time (on an equal area it is night).

Solar cells, photovoltaics, use solar power in the most direct way, converting it to electricity without intermediates such as steam or moving water. They need an external buffer technology (such as in the simplest case batteries) to synchronize their fluctuating energy supply with demand, but on the other hand, by working without any movable parts, they run silently and with very little wear, able to last several decades with little maintenance. While still a small part of the renewable-energy mix today, the market for solar-cell modules has been booming for several years now, seeing a growth rate of 50 % last year – the highest number among all renewable energies.

Among solar cells, the second-generation *thin-film* technologies are booming the most, and here the technology with the highest proven efficiencies (the current record for small cells being 20.3 % [26]) is the one based on $Cu(In,Ga)Se_2$ (copper–indium–gallium diselenide, CIGS). In this thesis, I investigate two fields of issues that offer potential improvements for CIGS thin-film solar cells.

1.1. Guide to the Content

Chapter 2 introduces the relevant concepts of solar-cell physics, discusses the principle of optical enhancement and presents CIGS thin-film solar cells in particular.

In **Chapter 3** we look at the various sample-characterization methods that were used in the course of my research. The techniques with which I want to make you acquainted here encompass electrical measurements of devices, optical measurements for determining the reflectivity of films, and an array of X-ray, electron-microscopy and ion-beam analyses of film composition, structure and morphology.

Chapter 4 concerns the methods by which samples were prepared and the resulting films. with the main weight on the *reactive sputtering* of zirconium nitride (ZrN) and on the *co-evaporation* of CIGS. Concerning the latter, I present a model of the autonomous ('intrinsic') development of gradients in a popular CIGS growth process and its impact on intentionally added ('extrinsic') gradients. A report of the comprehensive upgrade of the CIGS evaporator, to which I contributed to a large degree, is given in **Appendix A**.

Chapter 5 offers considerations firstly on how ZrN can be used as a reflecting back contact that could in the future allow for thinner devices yielding a similar power output as today's cells, and secondly on how various gradients influence the performance of CIGS devices, from which I derive recommendations on how to design gradient profiles.

In **Chapter 6**, I round off by summarizing my main findings and sketching out how they may be of future use.

2. Solar Cells

2.1. General

The basic solar-cell model.

A semiconductor solar cell is a *p–n* diode, for which in the dark the current density J obeys the diode equation

$$J(V) = J_0 \left(\exp \left(\frac{1}{n_{\mathrm{id}}} \frac{\mathrm{q}}{k_{\mathrm{B}} T} V \right) - 1 \right) \tag{2.1}$$

with the applied voltage V, saturation current density J_0, elementary charge q, Boltzmann constant k_{B}, temperature T and diode-ideality factor n_{id}. The saturation current density J_0 is determined by

$$J_0 = k_{\mathrm{B}} T \left(\frac{\mu_{\mathrm{e,p}} n_{\mathrm{i,p}}{}^2}{L_{\mathrm{e,p}} N_{\mathrm{A,p}}} + \frac{\mu_{\mathrm{h,n}} n_{\mathrm{i,n}}{}^2}{L_{\mathrm{h,n}} N_{\mathrm{D,n}}} \right) \tag{2.2}$$

where indices p and n stand for the *p* and *n* sides of the junction, respectively, and indices e and h stand for electrons and holes; μ is the carrier mobility, n_{i} the intrinsic carrier concentration, L is the diffusion length and N_{A} and N_{D} are the acceptor and donor concentrations.

In an illuminated diode, a photon with an energy higher than the bandgap E_{g} of the respective material is absorbed and generate an electron–hole pair (*generation*). This electron–hole pair may either be lost again at defects in the bulk or at an interface (*recombination*); but with a certain *collection probability*, it makes it to the terminals (electrodes) and contributes to the light-generated current density J_{ph} in the external circuit, which flows opposite to the normal, conducting direction of the diode. In the ideal case, J_{ph} depends only on the light's spectral composition and intensity, so that the current density coming out of the solar-cell device under a given illumination, simply is a superposition of Equation (2.1) and a constant term:

$$J(V) = J_0 \left(\exp \left(\frac{1}{n_{\mathrm{id}}} \frac{\mathrm{q}}{k_{\mathrm{B}} T} V \right) - 1 \right) - J_{\mathrm{ph}}. \tag{2.3}$$

The two equations (2.1) and (2.3) yield current–voltage curves as plotted in Figure 2.1. The illuminated current–voltage characteristics of a solar-cell device are summarized by four parameters: Open-circuit voltage V_{OC}, short-circuit current density J_{SC}, fill factor FF and efficiency η. With the
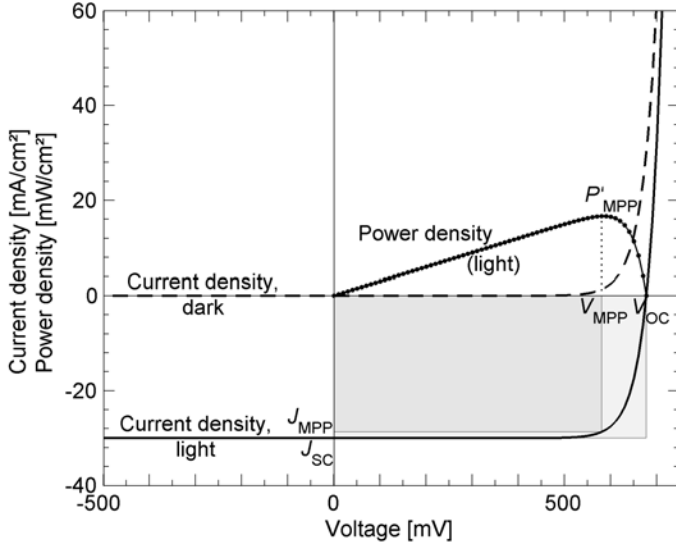
Figure 2.1: Plotted as functions of the applied voltage, the current densities of a dark and illuminated ideal solar cell and the power density under illumination. The maximum-power point P_{MPP} is marked, as are the associated current density J_{MP} and voltage V_{MP} spanning the inner of the marked rectangles, and the open-circuit voltage V_{OC} and short-circuit current density J_{SC}, which span the outer rectangle.

maximum-power point MPP defined as the point where the electrical power density $P' = V \cdot J$ delivered from the device is maximal, the fill factor becomes the quotient

$$FF = \frac{V_{MPP} \cdot J_{MPP}}{V_{OC} \cdot J_{SC}}, \tag{2.4}$$

and the efficiency then is

$$\eta = \frac{P'_{MPP}}{P'_{light}} = \frac{V_{OC} \cdot J_{SC} \cdot FF}{P'_{light}} \tag{2.5}$$

(P'_{light} being the light's power density, under standard testing conditions P'$_{light}$ = 100 mW cm^{-2}).

In the non-ideal real-world case, there are often three loss mechanisms to deal with, illustrated in the equivalent circuit in Figure 2.2: *Shunts*, which allow current to bypass the external circuit (causing an increase in slope around the short-circuit point); *series resistances*, which bring about a voltage drop under operation (causing the slope around the open-circuit point to decrease); and – particularly in thin-film solar cells – *voltage-dependent photo-current collection* [15,22], which invalidates the superposition principle named above.

6
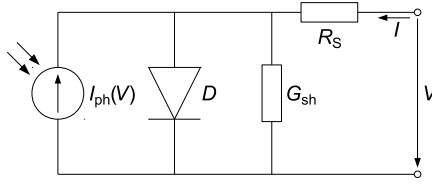
Figure 2.2: Equivalent circuit of a non-ideal solar cell according to the one-diode model, with the elements voltage-dependent light-current source $I_{ph}(V)$, diode D, shunt conductance G_{sh} and series resistance R_S.

At first glance at measurement data, voltage-dependent collection may be mistaken for a shunt, but it is generally easy to distinguish from it because it only affects the illuminated current–voltage curve [22].

This was a quick overview of the principles needed in the following discussions. A thorough introduction to the physics of solar cells is given in Martin Green's book "Solar Cells" [21].

Benefits of built-in fields.
If the diffusion length of minority carriers in the absorber is similar to or larger than the film thickness, there is a risk for these carriers to recombine at the rear contact – simply said, they may drop into the metal surface instead of going via the junction. This risk can be minimized by *passivating* the rear contact. One does this by building an electrical field ('back-surface field', BSF) into the material that bends the respective energy band such that the carriers are repelled from the interface. In conventional silicon solar cells, that band-bending is achieved by heavily doping the area around the contact. This also bends the other band such that the majority carriers are attracted to the contact, where they are supposed to go. In CIGS, we cannot replicate this procedure, since we have no direct control over the doping concentration, but in Section 2.3 we will learn of an alternative way to passivate the contact.

If the diffusion length is smaller than the film thickness, on the other hand, recombination at the rear loses its relevance, and the collection probability of the minority carriers becomes important: If electron–hole pairs are generated more than one diffusion length away from the junction, they run a high risk of 'wandering around' and recombining (this time in the bulk) before they make it to the junction. This, too, can be alleviated by an electrical field, this time preferably more spread out over the thickness of the absorber, so that the carriers get a shove towards the junction wherever they are in the film.

2.2. Optical Enhancement

Thin-film solar cells are feasible by virtue of the direct bandgap of the absorber material they use and the ensuing high absorption coefficient, as opposed to that of crystalline silicon, for instance. However, when the thickness of the absorbing layer is reduced further in an effort to reduce material costs, fabrication costs and/or bulk-recombination losses, one reaches a value where one pass of the light through the device does not suffice for complete absorption. A way to counteract these absorption losses is to employ optical enhancement, offering the impinging light effective path lengths that are greater than the absorber thickness. Optical enhancement, which is state of the art for instance in amorphous- and micro-crystalline-silicon solar cells, involves up to three strategies: Improvement of the reflectivity at the back of the device to minimize the optical losses; increased scattering to provide for diagonal light paths; and light trapping to avoid loss of reflected light through the window.

In Section 5.1 we will consider the material ZrN for the first of these applications, namely as a back-contact material with a higher-than-normal reflectivity. ZrN has a bright golden lustre and is both hard and chemically inert – properties which make it attractive for coating fashion items, for instance, but also for durable drill bits, valves in corrosive environments, oral implants and the like. The property that is important for our application is its high reflectance in the infrared, which is why ZrN also has been investigated for use in heat-mirroring window glass.

2.3. CIGS Thin-Film Solar Cells

Figure 2.3 shows a cross-sectional image of a $Cu(In,Ga)Se_2$ (CIGS) solar cell, taken by transmission-electron microscopy (TEM) and demonstrating the typical device structure: Placed on a bearing glass substrate, a 300 nm Mo back electrode is followed by a $Cu(In,Ga)Se_2$ (CIGS) film of 500 nm to 2500 nm thickness, which is the so-called *absorber* and constitutes the *p*-type side of the *p–n* diode. It is followed by a 50 nm thick CdS buffer, 50 nm of 'intrinsic' (unintentionally doped) ZnO and a 250 nm thick front electrode of strongly Al-doped (*n*-type) ZnO. The *p–n* junction is arguably formed within the top nanometres of the CIGS absorber [55], probably owing to a thin surface-defect layer (SDL) [48] which, though not forming a separate phase, is similar in composition and effect to the ordered-vacancy compound (OVC) $Cu(In,Ga)_3Se_5$ [31, 55].

CIGS is normally used as polycrystalline thin-films, although there do exist experiments with mono-crystalline samples grown on GaAs wafers, e. g. [52].

There are various types of processes possible and – to varying degrees – in use for fabricating CIGS absorbers. These include:
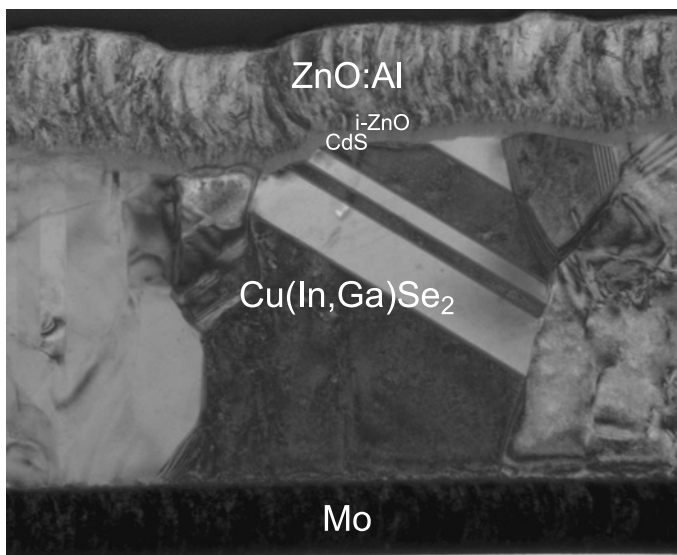
Figure 2.3: A TEM cross-section through a complete CIGS device. (Image courtesy of Timo Wätjen).

- Selenization and/or sulfurization of a stack or mixture of metallic precursors deposited by sputtering or evaporation [3, 34], or from ink-like fluids or pastes [30].
- Electro-deposition in a bath containing precursors for some or all of the components, followed, if needed, by selenization, sulfurization or thermal annealing [24, 37].
- Embedding in a polymer of CIGS particles deposited from an ink.
- Evaporation of the metals concurrently with selenium and/or sulfur onto a hot substrate, the so-called *co-evaporation*.

Only co-evaporation processes have been used for the CIGS films in this thesis. These processes in turn come in a range of varieties. The simplest form would be a *single-stage process*, where all the elements are evaporated at the same time and with constant rates (or at least constant ratios of the metals to each other). However, many modern processes intended for manufacturing devices incorporate a Cu-rich stage before turning Cu-poor (more on the reasons for this sequence below). The earliest example of this process form is the *Boeing* bi-layer process [49], and the two process types used in this thesis follow the same principle. The first type, our old baseline, can be viewed as a smoothed-out variant of the Boeing recipe, simulating an in-line fabrication where substrates move past fixed sources. The second type is the class of multi-stage processes (related to the NREL's three-stage process [12, 18]), which are widely used today and are responsible for all of the recent efficiency

world records [26, 51]. The specific implementations of both processes will be discussed in detail in Section 4.3.

The composition of a CIGS film is often specified using two ratios, the 'gallium content' and the 'copper content', which describe the number of atoms of the respective element relative to the total number of atoms from the third main group of the periodic system (the boron family, group 13 in the new IUPAC[1] nomenclature – in our case, indium and gallium): $[\mathrm{Ga}]/[\mathrm{In}+\mathrm{Ga}]$ and $[\mathrm{Cu}]/[\mathrm{In}+\mathrm{Ga}]$. In the literature, they are variously abbreviated with the symbols x and y (from the sum formula, $\mathrm{Cu}_y(\mathrm{In}_{1-x}\mathrm{Ga}_x)\mathrm{Se}_2$), Ga/III and Cu/III (using the older nomenclature of 'group III'), or GGI and CGI (from the initials of the considered elements). I stick to the latter pair – GGI and CGI – in this thesis. Let us consider why these ratios are relevant, and indeed most often sufficient.

Firstly, the gallium content GGI defines the bandgap of the CIGS absorber film. The bandgap is smallest for pure CuInSe_2 (GGI = 0) at 1 eV, largest – around 1.65 eV – for pure CuGaSe_2 (GGI = 1), and for intermediate values follows a linear relationship with a weakly quadratic downward-bending term: $E_{\mathrm{g}}(\mathrm{GGI}) = k + m \cdot \mathrm{GGI} - q \cdot \mathrm{GGI}(1 - \mathrm{GGI})$. When calculating the bandgap from the gallium content, we have used the data determined by Alonso et al. [1] and cited by Shafarman and Stolt [56]:

$$E_{\mathrm{g}}(\mathrm{GGI}) = 1.01 + 0.626 \cdot \mathrm{GGI} - 0.167 \cdot \mathrm{GGI}(1 - \mathrm{GGI}) \qquad (2.6)$$

The gallium content for the theoretical optimal bandgap of 1.3 eV [23] thus would be approximately 50 %. Also, the change in the bandgap takes place (practically) only in the conduction band, that is to say, it is the position of the conduction-band edge (relative to the vacuum level) that depends on the gallium content. That means that it is possible to shape the conduction band by including different amounts of gallium at different depths in the absorber. The high efficiency of three- and multi-stage processes is to a good part attributed to the tendency of the processes 'intrinsically' to cause the formation of a Ga profile that is commonly called the 'notch', namely a lower Ga concentration sandwiched between two regimes of increasing concentration. It was first suggested by Eron and Rothwarf in the 1980s [15, 16] that this kind of structure would be beneficial for CuInSe_2 solar cells, and later experimental evidence by Dullweber and co-workers [13] confirmed this view. Put briefly, a higher bandgap at the *p–n* junction offers a chance to reduce recombination in the space-charge region (SCR) by virtue of reducing the intrinsic carrier density; a smaller bandgap deeper in the absorber allows the absorption of more long-wavelength light; and the rise towards the back contact presents a passivating or electron-pushing back-surface field as introduced in Section 2.1.

Secondly, the copper content CGI is primarily important for the electronic viability of the material. A value of CGI = 1.0 signifies *stoichiometry*, that

---

[1] IUPAC: International Union of Pure and Applied Chemistry

is, that the metals are present in an equal ratio as given by the sum formula $Cu(In,Ga)Se_2$. Stoichiometric and under-stoichiometric CIGS (material with CGI $\leq$ 1) has a high resistivity, but over-stoichiometric CIGS (material with CGI $>$ 1) tends to be rather conductive due to segregated Cu_2Se, which has metal-like resistivities around or below $0.1\,\Omega\,cm^2$ [57]. For the performance of devices, this low resistivity easily becomes devastating since it leads to shunting (see Section 2.1). Therefore, finished absorber films have got to have a CGI value below 1, although many CIGS-growth processes do include a period with over-stoichiometric copper content, as the Cu_2Se phase is considered to be liquid and promote the growth of larger crystal grains [60]. The typical final value of the average CGI for good CIGS devices is in the range between 80 % and 95 %, though even much more copper-poor material is able to yield working devices. In fact, as I mentioned further above, a very copper-poor composition around CGI $= 1/3$ forming the beneficial SDL is often found at the very surface of good CIGS devices.

SCAPS modelling.
In Paper V, we employed electrical modelling with the software tool SCAPS [9] to gain a deeper understanding of the effects of In-enhancement at the surface. SCAPS allows the definition of thin-film solar-cell devices as one-dimensional stacks of layers with a large set of parameters and solves the fundamental solar-cell equations (the Poisson equation and the continuity equations for electrons and holes) for each point. Definable parameters include the doping, defect and interface-state densities and cross-sections, the optical absorption coefficient, the bandgap and the electron affinity. In recent versions of SCAPS [8], many of the properties can be specified as gradients of various forms. Our model built upon a baseline model for graded CIGS recently developed in our group [46]. We adapted it to the GGI profiles found in my devices by emulating the basic notch profile as a parabola with suitable support points, and altered a number of properties in this reference model to fit the observed solar-cell parameters before additionally emulating the front-surface modifications as linear slopes.

Figure 2.4 shows the energy-band diagram of a fairly straight-forward (ungraded) CIGS device. The figure has been generated with SCAPS and demonstrates the basic layout of the heterojunction, with a typical space-charge region width of about $0.4\,\mu m$ and a small positive conduction-band offset (CBO) between the CIGS and the CdS buffer as it is widely assumed to exist [42]. Not included in this diagram are the effect of a $MoSe_2$ layer at the Mo/CIGS interface and of an SDL at the CIGS/CdS interface. The former is assumed to constitute a thin layer with slightly raised conduction-band and valence-band edges, the latter, to widen the bandgap by around $0.3\,eV$ relative to CIGS by lowering the valence-band edge.
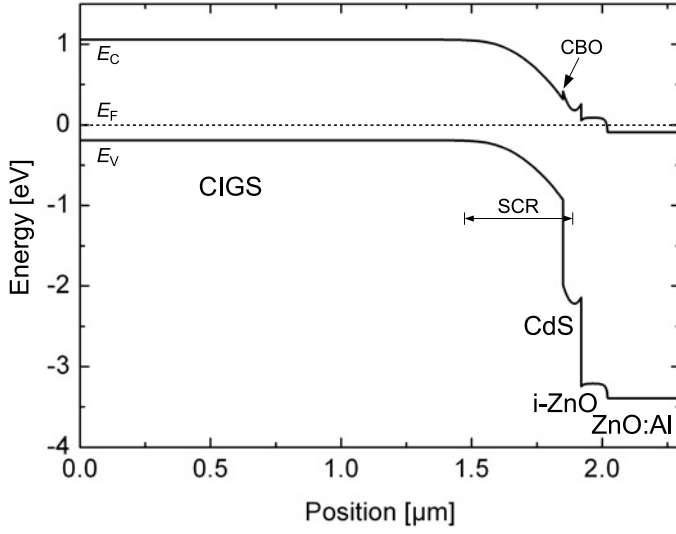
Figure 2.4: The energy-band diagram of a simple CIGS device, whose absorber does not include a gallium gradient. Besides the layers as presented above (the Mo back contact would follow at the left), we have marked out the valence-band edge E_V, the conduction-band edge E_C, the Fermi level E_F, the conduction-band offset CBO between absorber and buffer, and the approximate extent of the space-charge region SCR. (Diagram courtesy of Jonas Pettersson.)

3. Characterization Methods

This chapter deals with various characterization methods that have been relevant in my studies. In continuation of the discussion of electrical properties of solar cells, I will begin the chapter with two electrical analyses. The following section deals with the optical evaluation used with the ZrN films. X-ray-based methods yielded information about average composition (XRF), surface composition (XPS) and crystal structure (XRD), and electron microscopy was used to create images of top views and cross-sections of samples. Last but certainly not least, ion-beam analyses allowed me to observe depth profiles of my thin films.

   A few auxiliary analyses are not given their own sections: Where needed, the thickness and roughness of films were determined with a *Dektak V 200-Si* profilometer, and the electrical resistivity of samples was measured with a four-point probe setup.

3.1. Electrical Analyses

3.1.1. Current–Voltage Measurements

Current-density–voltage (JV) measurements are the standard method for evaluating the electrical performance of solar cells. The device under test is placed under a light source approximating the normalized AM 1.5 sun spectrum [2]. Through one pair of probe needles, the voltage across the device is swept through an appropriate range and the current is measured, while the precise voltage is measured over a neighbouring pair of probes. This four-point probe setup largely avoids measurement errors owed to probe-contacting resistances. In this work (in all papers except for Paper II), an *ELH* halogen projector lamp was used as the light source.

3.1.2. Diode-Model Evaluation

For Papers III and VI, the parameters of the one-diode model – shunt conductivity G_{sh}, series resistance R_{S}, saturation current density J_0 and ideality factor n_{id} – were extracted from measured JV data using the evaluation method suggested by Hegedus and Shafarman [22], which was developed especially with thin-film solar cells in mind. This method does not fit all four parameters at once but rather splits up the analysis into three steps:

Shunt conductivity.

In the first step, the ohmic shunt conductivity G is estimated from the *differential* conductivity $g = \Delta J / \Delta V$ at negative bias voltages, where the ideal diode's contribution is negligible. In our case, this signal was rather noisy, so we used the average of g as the estimator of G, rather than the minimum value as suggested in the original paper.

Series resistivity & ideality factor.

In the next step, the current density is freed from the influence of the shunt by defining $J_{\text{diode}} := J - GV$, and then the function

$$r(J) = R + \frac{k_{\text{B}}T}{q} \cdot n_{\text{id}}/J \qquad (3.1)$$

with Boltzmann constant k_{B}, temperature T and ideality factor n_{id}, is fitted numerically to the measured differential resistivity $r = \Delta V / \Delta J$ with J_{diode} as the function argument, or for the illuminated curve, with $J_{\text{diode}} - J_{\text{SC}}$. When plotted as a function of the inverse of the adjusted current density, for sufficiently high current densities (above approximately $0.1 \cdot \max(J)$), the above function yields a straight line with the series resistivity R as the y-axis intercept and the ideality factor n_{id} of the diode proportional to the slope.

Saturation current density & ideality factor (again).

Finally, the diode equation (2.1) can be fitted to the adjusted current density (as before, in the illuminated case offset by J_{SC}) as a function of the voltage $V_{\text{diode}} := V - RJ$ which drops across the idealized diode free from series-resistance losses. A plot of this function with a logarithmic y-axis yields a straight line intercepting the y-axis at J_0 and with the ideality factor again easily extracted from the slope. My fitting algorithm actually uses the ideality factor obtained from the resistivity fit as a fixed input parameter, so that the determination of the saturation current density is decoupled from the determination of the ideality factor.

3.1.3. Quantum Efficiency

The quantum efficiency (QE) describes the probability of an impinging photon of a certain wavelength to create an electron–hole pair that is successfully collected at the terminals of the device. A QE analysis provides insights into wavelength-dependent absorption and collection, as well as a correction of the spectrum mismatch in JV measurements.

QE (strictly speaking, external quantum-efficiency or EQE) measurements feature in all included papers (albeit only for demonstration purposes in Pa-

per II), the data being recorded in ambient light[1], with the monochromatic light being provided from a Xe-arc lamp via a sequence of monochromator, chopper and optical fibre and scanned over a range of 360 nm to 1200 nm in 10 nm steps.

3.2. Optical Analyses

In Papers I and II, we measured the specular reflectance of ZrN films and complete devices. For this we used the very setup described in detail by Nostell and collaborators [44] in its 'absolute-instrument' configuration, where 'absolute' refers to the fact that in this case, the final result is obtained without further calibration, by dividing (at each wavelength) the reflected intensity by the intensity measured in a reference run where the sensor is placed directly in the light path without a sample in between. As with QE above, the wavelength of the monochromatic light was scanned in steps of 10 nm between 360 nm and 1200 nm.[2]

While the reflectance characteristics were measured in air, the most relevant property for assessing the reflector material is its reflectance within the solar-cell device. To calculate the reflectance at a given interface, we have to know the complex refractive indices $\underline{N}$ of the two materials on either side of the interface:

$$\underline{N} = n - \mathrm{j}k = \sqrt{\underline{\varepsilon}_r} \tag{3.2}$$

with the real part of the refractive index n, the extinction coefficient k and the complex dielectric function $\underline{\varepsilon}_r$.[3] Under the condition that the materials are non-magnetic (which all materials relevant here are), and for perpendicular incidence ($\alpha = 90°$), the reflectance at the interface between them is then governed by the following simplified form of the Fresnel formula [33, ch 3.1.4]:

$$R(\omega) = \frac{|\underline{N}_1(\omega) - \underline{N}_2(\omega)|^2}{|\underline{N}_1(\omega) + \underline{N}_2(\omega)|^2} = \frac{(n_1(\omega) - n_2(\omega))^2 + (k_1(\omega) - k_2(\omega))^2}{(n_1(\omega) + n_2(\omega))^2 + (k_1(\omega) + k_2(\omega))^2} \tag{3.3}$$

For the refractive index of $CuIn_{0.77}Ga_{0.23}Se_2$ we use data from Orgassa et al. [45, App. B], and for molybdenum, data from the CRC Handbook [35, Section 12]. The refractive index of air is approximately equal to 1.0 (independent of wavelength).

---

[1] I use the expression 'in ambient light' specifically to mean on the one hand, that the measurements occurred in a normally lit laboratory room, not a closed 'black box' or a darkroom, and on the other hand, that no direct bias light was used either.

[2] Since a change of the detector and manual start of a new measurement were necessary for wavelengths over 1100 nm, and since the long-wavelength reflectance of ZrN had early on proven entirely monotonic, the ZrN measurements were usually terminated at 1100 nm.

[3] The symbol 'j' stands for the imaginary unit.

What remained for myself to determine was the refractive index of zirconium nitride. For this I utilized the fact that zirconium nitride is well described by the screened Drude model of free-electron metals [5, 62], which provides the following equation for the complex dielectric function $\underline{\varepsilon}_r$ for visible and infrared radiation:

$$\underline{\varepsilon}_r(\omega) = \varepsilon_\infty - \frac{\omega_P{}^2}{\omega^2 + j\omega/\tau} \tag{3.4}$$

with the high-frequency dielectric constant ε_∞, the plasma frequency ω_P and the scattering time of electrons τ. The parameters of the dielectric function of zirconium-nitride films are determined by making a least-square fit of Equation (3.4) to the measured reflectance data in air via Equations (3.3) and Equation (3.2):

$$R_{\text{fit}}(\omega, \omega_P, \tau, \varepsilon_\infty) = \frac{|\sqrt{\underline{\varepsilon}_{r,\text{ZrN}}(\omega, \omega_P, \tau, \varepsilon_\infty)} - 1|^2}{|\sqrt{\underline{\varepsilon}_{r,\text{ZrN}}(\omega, \omega_P, \tau, \varepsilon_\infty)} + 1|^2}. \tag{3.5}$$

3.3. X-Ray Analyses

3.3.1. X-ray Fluorescence

X-ray fluorescence (XRF) provides quantitative compositional data and is our standard method for determining the overall composition of CIGS samples. We used it for this purpose in all of my papers except for Paper II, where the areal atom density (number of atoms per unit area) of Zr was determined by it instead, serving as a proxy measure for the film thickness in samples where no profilometer measurement was possible.

The measurements were carried out in a *SPECTRO X-LAB 2000* system, in which the primary X radiation is first directed onto one of several *targets*, before being used to stimulate the sample itself, and the evaluation is energy-dispersive by means of a semiconductor sensor. We use a Mo secondary target for Cu, Ga, Se and Zr, and an Al_2O_3 scattering target for In.

A Teflon-and-metal blind in front of the sample blanks out the relevant X-ray radiation outside a circular aperture area of 1 cm diameter. The measurement volume extends several μm into the sample. Quantification is performed by means of a linear model for the relation between detector counts and atomic concentrations and is calibrated with a reference sample of known composition and film thickness. The measured spectra are semi-automatically imported into a database, from where they can be used directly in other evaluations such as those of BAK processes (Section 4.3.1, Appendix A) or SIMS depth profiles (Section 3.5.1 below).

3.3.2. X-ray Photoelectron Spectrometry

In Paper V, we used X-ray photoelectron spectrometry (XPS) to measure the Ga content at the surface and to get an estimation of the degree of surface oxidation. The analysis, also called electron spectroscopy for chemical analysis (ESCA), is a surface-sensitive method for detecting the presence, concentration and chemical binding state of elements, observing only the topmost few nanometres of the film. Photoelectrons are excited by means of monochromatic X-rays with a fairly low energy in the range of 1 keV, usually Mg–K$_\alpha$ (1253 eV) or Al–K$_\alpha$ (1486 eV) radiation.

Our XPS study was carried out in a *Quantum 2000 Phi* instrument that employs Al–K$_\alpha$ radiation. In order to measure on surfaces that were degraded by air exposure as little as possible, we deposited a protective CdS cover film (a standard buffer layer, see beginning of Chapter 4) on all newly grown CIGS samples within 15 minutes of unloading them from the vacuum chamber, and about five minutes before loading the samples into the XPS system, etched this film away with dilute HCl of 3 % concentration and blow-dried the samples with nitrogen. The data were collected from the Ga–L$_3$M$_{45}$M$_{45}$ Auger peak at 421 eV and the In–3d$^{5/2}$ peak at 445 eV, by which we aimed to avoid interference with other surface peaks. The concentrations were calculated from the respective peak areas with sensitivity factors determined by matching to the XRF-calibrated SIMS surface data on the reference piece.

3.3.3. X-ray Diffraction

X-ray diffraction (XRD) yields information about the presence, orientation and quality (grain size) of crystallographic phases. Owing to the principles of constructive and destructive interference, for a given X-ray wavelength, each angle for which a significant diffracted intensity is detected corresponds to a particular distance of diffracting crystal planes.

$\theta/2\theta$-XRD shows the preferential orientation of grains with respect to the sample surface, with a penetration depth of several micrometres. Grazing-incidence (GI) X-ray diffraction shows the distribution of unordered crystal structures not parallel to the surface, and by keeping the angle of incidence close to or below the critical angle, the measurement can be made rather surface sensitive with a penetration depth in the order of mere tens of nanometres.

The analyses in this thesis were carried out in a *Philips X'pert MRD* diffractometer, which uses Cu–K$_\alpha$ radiation with a wavelength of 1.54 Å, works in a non-focusing geometry and is furthermore equipped with an X-ray mirror and an 0.09° parallel-plate collimator. In Paper II, both methods were employed to investigate the phase composition and crystallinity of ZrN films. In Paper V, $\theta/2\theta$-XRD data confirmed that all samples had good crystalline quality and very comparable textures, and in Paper VI, $\theta/2\theta$-XRD diffractograms verified the development of phase composition while GI-XRD data helped to verify the presence of Cu$_2$Se at the surface.

3.4. Electron Microscopy

In Paper III, we examined several samples by transmission-electron microscopy (TEM) to investigate the size of the CIGS grains and detect possible defects or splitting of grains due to strong gradients. We also performed an electron-diffraction analysis to check for a possible defect-chalcopyrite layer, and furthermore recorded compositional line scans by energy-dispersive X-ray spectroscopy (EDX) in scanning TEM (STEM) mode as a cross-check for SIMS depth profiles (see Section 3.5.1).

EDX is a compositional characterization method similar to XRF, the main difference being that in EDX, the X-ray radiation is generated by the direct interaction of the electron beam of an electron microscope with the sample. The electron beam excites X-rays in a pear-shaped volume typically a few micrometers deep and several micrometres across under the surface, which reduces the spatial resolution severely. For this reason, EDX usually only provides sufficient spatial resolution for meaningful depth profiling of cross-sections when used on electron-transparent samples, particularly in TEM.

The TEM studies were primarily carried out on a *FEI Tecnai F30 ST* microscope. The samples were prepared according to the so-called *classical* method, gluing small sample pieces face to face with epoxy glue, then polishing down to ca. 80 µm, dimple-grinding on both sides down to about 10 µm in the center of the dimples, and thinning to electron transparency by precision ion polishing at low incident angles with final ion energies of about 1.5 keV.

Scanning electron microscopy (SEM) images were recorded on a *LEO 1550* microscope equipped with a field-emission gun operated at various acceleration voltages between 3 keV and 15 keV. Cross-section images of cleaved samples were used in Paper V to compare grain sizes. In Paper VI, SEM was used on the one hand for top-down images of sputter craters, on the other hand for cross-sections of samples that had been polished by a partial (one-sided) application of the classical TEM-preparation method described above.

3.5. Ion-Beam Analyses

3.5.1. Secondary-Ion Mass Spectrometry

In secondary-ion mass spectrometry (SIMS), a beam of primary ions, with impact energies of a few keV, is swept over a defined area on the sample surface and sputters away atoms and ions from the sample, gradually creating a crater. The expelled ions, called the *secondary ions*, are extracted and their rate counted, cyclically detecting one species at a time. Thus the raw results of a SIMS analysis are countrate profiles as functions of sputter time.

SIMS was used in Papers III, V and VI to record depth profiles of the constituent species of CIGS (that is, Cu, In, Ga and Se). The instrument used

was a *Cameca IMS 4f* system, and Cs⁺ ions with an impact energy of $4.5\,\mathrm{keV}$ served as the primary ions.

Given appropriate boundary conditions and means of calibration, it is possible to translate these countrate profiles into profiles of atomic concentrations as functions of depth in the film. The main prerequisite for a valid compositional calibration is that the erosion rates and the ionization probabilities of all the relevant elements be largely constant within the investigated film or at worst, vary in a consistent manner. In the general case, the ionization probability of an atom species in SIMS may depend strongly on the chemical environment from which it is being sputtered. This complication is known as the *matrix effect* and tends to be particularly severe when sputtering with oxygen O⁻ primary ions, in which case it can cause signals to vary by more than an order of magnitude between two materials.

The matrix effect can be mitigated by making use of another effect, namely the fact that not only atomic secondary ions but also various molecular ions are expelled from the sample, including molecular ions MP⁺ consisting of the primary projectile P and the investigated atom species M, and that the formation probability of these latter ions turns out to be fairly independent of the material they originate from. Although this probability understandably is much smaller for molecular ions than for the elemental ones, the resulting countrates are usually entirely sufficient to achieve a good compositional resolution (for instance, in our measurements we typically got around 1×10^5 counts per second). Therefore an established technique for avoiding the matrix effect consists in sputtering with caesium Cs⁺ ions and detecting molecular ions MCs⁺ [20]. All the SIMS analyses in this work were carried out using this technique.

One way to calibrate SIMS data quantitatively would be to measure by SIMS a reference with a known composition. However, I chose to calibrate each sample with its own XRF data. For this, a correction factor was calculated for each atom species by comparing the sum of the SIMS count-rate profile of that species with the corresponding average atomic content that was returned by the XRF measurement, in a way analogous to that described at the beginning of Section 4.3. Applying this factor to every point of the original profile yields a profile of atomic concentrations.

In Paper III, we successfully verified this calibration method by also recording depth-profile TEM-EDX line scans on two samples. The absolute levels of the EDX data were different at that time, since they were computed from first principles and not calibrated with an actual reference, but the shapes of the profiles were very comparable between the two methods.

The depth resolution of a SIMS analysis is limited on the one hand by so-called *cascade mixing* and on the other by surface roughness. Cascade mixing describes the effect that the primary ions not only affect the topmost atomic layer of the sample, but rather induce a cascade of collisions of sample atoms being kicked out of their lattice sites. Owing to this, any secondary ion de-

tected at a certain time may originate from the current sample surface or from some way below, which in turn may be the ion's original position, or its position after some displacement due to earlier bombardment. Mathematically, this situation can be described as an exponential decay. This is why the depth resolution in SIMS is often quantified in terms of the so-called *exponential decay length*. One determines the decay length at the trailing edge of the transition of one layer to another according to the equation [39]

$$\lambda_d = \frac{z_2 - z_1}{\ln(I(z_1)) - \ln(I(z_2))} \tag{3.6}$$

where z_i are two appropriately chosen points on the edge and $I(z)$ is the intensity at point z.

With atomically flat samples such as single-crystalline silicon, the decay length is only owed to cascade mixing and lies typically in the range of 5 nm to 10 nm [38]. Surface roughness, or more generally interface roughness, is naturally present in multi-crystalline samples such as ours and further decreases the depth resolution. Topology effects may augment the initial roughness and impact on the resolution, as may the inhomogeneous distribution of a layer sputtering at a considerably different rate than its neighbour.

Figure 3.1, comparing the uncalibrated SIMS profiles of two samples, demonstrates as an example the problem that the presence of Cu_2Se at the surface can pose for a SIMS analysis in this way. The sample in the upper figure consists of a finished, Cu-poor CIGS film on top of a Mo film and the signals within the CIGS region are largely flat, apart from the valley-like grading in the Ga and In signals, which are expected and will be discussed in detail in Section 4.4. In contrast, the sample in the lower figure is Cu-rich, and other analysis methods indicate that there is Cu_2Se on top of the CIGS. It is also known since earlier [14, 54] that Cu_2Se in Cu-rich CIGS samples forms both on the CIGS surface and in grain boundaries. Here, the Se and Cu signals are strongly increased over a considerable range at the beginning of the measurement, and although the film is grown on Mo of the same roughness as the first one, the decay lengths of the CIGS signals are several times as large. Electron-microscopy and profilometer analyses in Paper VI show that the crater floor is much rougher on the Cu-rich sample, being littered with columnar remains of the CIGS film. These observations suggest strongly that the Cu_2Se layer erodes at a lower rate than the CIGS film – though conceivably with higher ionization probabilities – and protects the CIGS film for shorter or longer periods, depending on its own local thickness, creating a rather rough surface that propagates along with the sputter front.
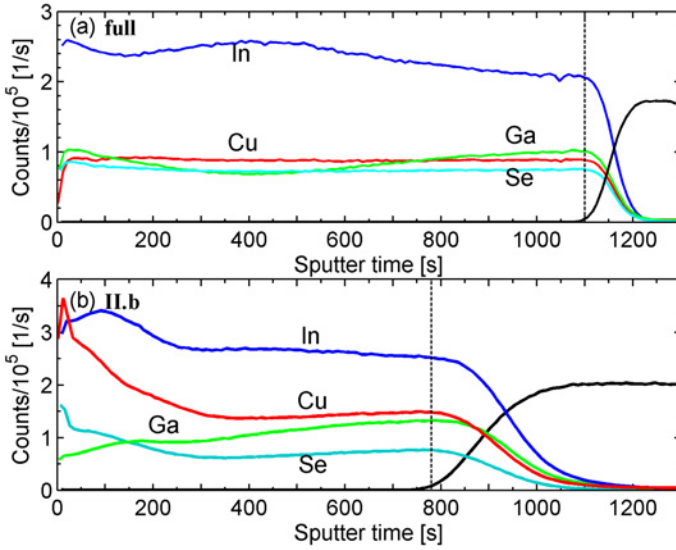
Figure 3.1: SIMS count-rate profiles of two reference samples: (a) full absorber, (b) Cu-rich sample – CIGS capped with Cu_2Se. In case (b), the Cu and Se counts are strongly elevated at the front, and the transition from CIGS to Mo takes more than three times as much time as in (a). The dashed vertical lines indicates the times above which we have considered counts as not belonging to the CIGS layer.

3.5.2. Elastic Recoil Detection Analysis

In elastic recoil detection analysis (ERDA), an ion beam with an energy in the MeV range is directed into the sample. In contrast to SIMS, secondary ions are not only ejected from the very sample surface and closely below, with depth information being owed to the development of a crater, but rather from a volume up to several µm deep. The depth from which an ion detected in ERDA has originated can be derived from its kinetic energy. In Time-of-flight energy (ToF-E) ERDA, which was used for studying Zr-N samples in this thesis, this information is decoded from the ion's time of flight between two detector foils, that is, from its speed. Also in contrast to SIMS, ERDA allows the extraction of fairly quantitative composition data without further calibration. We estimate that the measurement error is in the order of 6 % of the elemental ratio value.

ERDA works well for detection of all elements lighter than the primary projectiles. The ERDA depth analyses of my ZrN samples for Paper II were carried out at Uppsala University's Tandem Laboratory with 40 MeV $^{127}I^{9+}$ ion projectiles, and they were thus well suited for analysing the distribution of both relevant component elements, ^{91}Zr and ^{14}N. Figure 3.2 shows a typical depth profile recorded by ERDA.
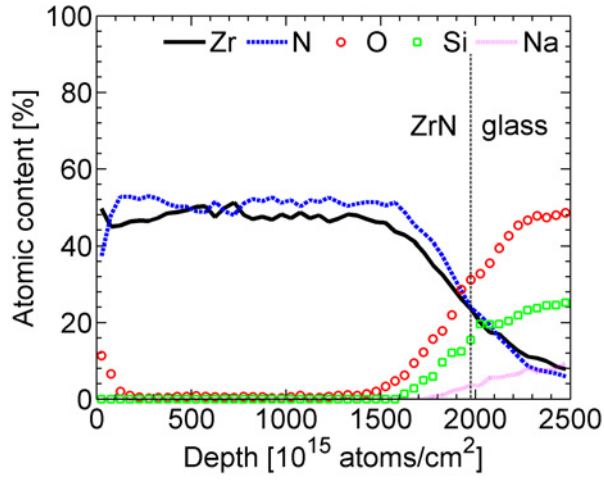
Figure 3.2: ERDA atomic-content profiles of the elements Zr, N, O, Si, and Na in Zr-N sample number II in Paper II. The x-axis unit of 1×10^{15} atoms/cm^2 corresponds to one monolayer. The increase of the oxygen signal near 0 hints at surface oxidation. The dashed vertical line marks the actual border between the film and the glass, which is smeared out in the data due to the limited depth resolution of ERDA. The Zr and N signals are fairly uniform and close to a ratio of N/Zr = 1, and thereby corroborate several other analyses which all indicate stoichiometric material in this case.

4. Preparation Methods

In this chapter we look at the process steps involved in preparing the CIGS-device stack that I showed earlier on in Section 2.3.

The most relevant techniques for my studies, and thus deserving the most extensive treatment, have been the reactive sputtering of zirconium nitride and the co-evaporation of CIGS, the latter in one particular machine of ours, affectionately known by its acronymous name as "the BAK". The non-reactive sputtering of the molybdenum and the zinc oxides gets a somewhat extended description by virtue of its being the 'parent technology' of the reactive sputtering.

That leaves a few components and steps of our Baseline process flow to fall a bit by the wayside, being necessary for the device but of no particular relevance for the studies I present here. In brief, my substrates are 1 mm thick sheets of soda-lime glass, cleaned in ultrasonic baths first with and then four times without a detergent and finally spin-dried. The buffer employed here consists of CdS prepared from the ingredients thiourea, cadmium acetate and ammonia by chemical bath deposition (CBD) taking ca. 8 min at a bath temperature of 60 °C. The grid, a 'fork' with a contact pad and two tapered prongs that in total shades 2.5 % of the cell area, is deposited onto the doped zinc-oxide film by electron-beam evaporation in the sequence nickel (ca. 50 nm)—aluminium (ca. 2 µm)—nickel (ca. 50 nm). Cells of 0.5 cm^2 are defined around the grid forks by automatized mechanical scribing with a needle that removes the zinc oxide, buffer and CIGS but leaves the molybdenum intact.

4.1. Sputtering

Simply speaking, sputter-deposition entails generating a plasma, a gas of charged particles (ions and electrons), in front of an area of the material to be deposited (the *target*), directing the gas ions towards the target in an electrical field so that they knock out ions and (predominantly) atoms from it, and placing one's substrate at a small distance opposite the target so that these eroded particles land on the substrate [53]. Some of the advantages of sputtering compared to evaporation are the fact that particles arrive at the substrate with a high kinetic energy – typically several eV –, which leads to good adhesion and denser film structure, the capability to deposit materials

having a low vapour pressure, which are difficult to evaporate, and the relative ease of scaling up. All the sputter-deposition processes described in the following are forms of the so-called *magnetron-sputtering* process [59]. This is the most common technique today and has a high yield, since a permanent magnet placed behind the target forces the electrons of the plasma to gyrate on a closed loop close to the target surface, preventing them from quickly being lost to the rest of the chamber. The high sputter yield allows process pressures typically to lie around 1×10^{-3} mbar to 1×10^{-2} mbar, giving the particles a sufficiently long mean free path to avoid their thermalization (loss of kinetic energy) and at the same time helping ensure high purity of the deposited films, since a low gas throughput spells a reduced risk of introducing impurities.

4.1.1. Non-reactive Sputtering

Three of the layers in the standard CIGS device structure are deposited by non-reactive sputtering in argon: The molybdenum rear contact, the intrinsic zinc-oxide (ZnO) window, and the aluminium-doped zinc oxide making up the front contact. Here each target consists of the very material to be deposited and the glow discharge is ignited in a pure argon atmosphere. As argon is a noble gas, it just transfers kinetic energy to the atoms in the surfaces it erodes, but does not react with them.

Molybdenum is electrically conducting and therefore direct-current (DC) sputtering can be employed for it, which is the fastest process and the one easiest to handle. Direct current means that a constant (negative) voltage is applied to the target.

With insulating target materials, on the other hand, sputtering with direct current would quickly leave the target surface charged, as positive ions would be impinging on the target all the time, and this charge build-up would bring the deposition to a halt [53]. The situation is again different with poorly conducting targets such as our intrinsic zinc oxide, where a charge build-up on the target surface can cause *arcing*, a localized discharge towards the target's backing plate through the target, which over time will damage the target. In both named cases, one must therefore apply an alternating voltage to the target. Doped zinc oxide lies between molybdenum and intrinsic zinc oxide conductivity-wise, and is usually sputtered in the same way as intrinsic zinc oxide.

In our group, the molybdenum is deposited in a *MRC* in-line system, which has a pallet with the substrate(s) slowly moving past the vertical, 30 cm high target. The two zinc oxides are either deposited in the same system (using pulsed DC sputtering), or in a smaller lab-scale system, a *von Ardenne CS 600 S*, where the samples during deposition are placed statically underneath circular targets of 5" diameter and radio-frequency

(RF) sputtering is used. All devices in the studies presented in this book are prepared with zinc oxides from the *von Ardenne* sputter.

4.1.2. Reactive Sputtering

In contrast to the non-reactive sputtering I have described so far, the ZrN films are fabricated by *reactive* sputtering. Here the target consists of elemental metal (in our case, zirconium), and a reactive gas (nitrogen) is added to the conventional argon working atmosphere. In contrast with the argon ions, the nitrogen ions also interact chemically with the target as they are implanted into it, forming a thin layer of a nitrogen-containing compound on its surface [28]. We will take advantage of this fact for diagnostic purposes. From that altered surface layer of the target, material is eroded by the plasma as before and eventually condenses on the substrate (and other exposed surfaces), where it may react further with nitrogen from the atmosphere.

Our deposition of ZrN was carried out in a *von Ardenne CS 730 S* sputter system where the samples of up to 10 cm side length lie still underneath 6"-diameter targets for the duration of the deposition.

Hysteresis.

In the general case, the control of a reactive sputter process is complicated by the existence of a hysteresis effect with respect to the flow of the reactive gas [6]. The hysteresis effect limits the achievable compositions or decreases the deposition rate substantially. In a typical process, two distinct operating modes exist: When the flow of reactive gas is low, the target surface is kept metallic and the deposition rate is high, but the deposited films are under-stoichiometric. For higher reactive-gas flows, the target gets covered with a compound due to the reaction with reactive gas, which results in a low deposition rate. Possibilities for suppressing the hysteresis, so that one can explore the whole area of compositions and working conditions, include applying feedback control to the reactive-gas flow and using a high pumping speed [29]. We found that the pumping speed in our sputter chamber was high enough so that no further steps were needed to avoid the hysteresis. A technique such as feedback control would probably have to be employed in a industrial-scale system.

Sputter condition.

Steady-state sputtering operation requires that the number of ion particles in the plasma be constant. As laid out by Lieberman and Lichtenberg [36, Ch. 14.5], ions are generated in a cascade process, where ions impinging on the target cause the emission of *secondary electrons* with a yield γ, which in turn each create N new ion-electron pairs in the plasma. Consequently, the steady-state condition can be described by the relation $N \cdot \gamma = 1$.

The electron-emission yield γ is primarily dependent on the target material, and like the sputter rate, it is sensitive to surface composition. It is thus this coefficient that varies as the target changes from metallic state to compound state.

The ion yield N is approximately proportional to the target voltage U and depends on various properties of the sputter atmosphere, such as the gas composition and the pressure, increasing with increasing pressure. The pressure dependence can be attributed to the reduction of the mean free path of electrons with increasing pressure, which enhances the probability of ionising a gas atom.

Rewriting the steady-state condition as

$$N^* \cdot \gamma \cdot U = 1 \tag{4.1}$$

– where N^*, of the dimension V^{-1}, is the voltage-independent part of the ion yield –, we see that the target voltage correlates with the target state. As Sproul et al. [58] indicate, the transition from metallic mode to compound mode is indicated by a local extremum of the voltage as a function of the reactive gas flow.

If the discharge current is increased, the total number of ions eroded from the target increases as well, and thus a higher flow of the reactive gas is needed for maintaining any given target state.

Other factors influencing the actual value of the target voltage include the geometry of the sputtering chamber, which encompasses the current position of the shutter and the depth of the race track on the target. Thus, one cannot derive a general formula for evaluating the target state based on the voltage alone; nonetheless, the *relative* voltage does provide a way to the needed information.

Experimental determination of the working point.

We have so far discussed in relatively abstract terms how the target voltage is connected with the compound state of the target. We can verify those findings by looking at Figure 4.1, which shows the development of the target voltage as the result of sweeps of the nitrogen gas flow at different argon gas flows and discharge currents. While the voltage level itself changes with the varying settings, and indeed depends on whether the nitrogen flow has previously been higher or lower, it is clearly seen that for different argon flows (the graphs in the top figure), the peak in the voltage stays roughly at the same position on the nitrogen-flow axis, and that for different currents, it shifts in a consistent manner. Investigating a range of $3\,\mathrm{A}$ to $6\,\mathrm{A}$, we found that the flow for the voltage maximum could always be described as $Q_{\mathrm{N}}^*/(1\,\mathrm{sccm}) = 4 \cdot (I/(1\,\mathrm{A}) - 1)$. The analyses presented in the following section will show that stoichiometric ZrN films are achieved at the very gas flow indicated by the peak.
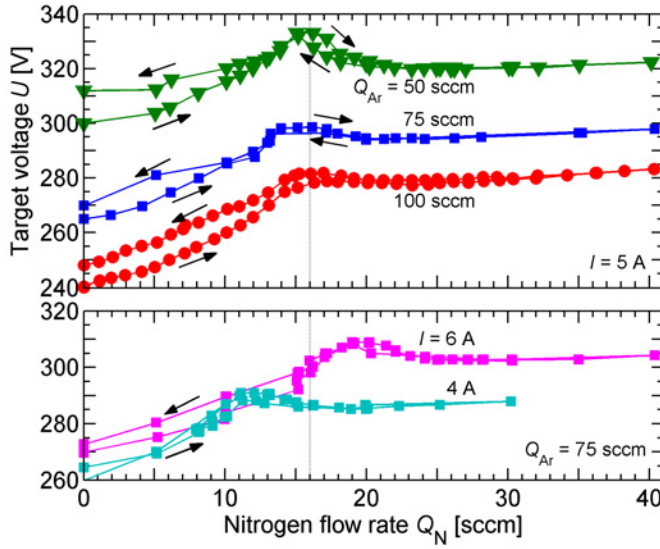
Figure 4.1: Target voltages as functions of the nitrogen flow. **Top**: For constant discharge current and three different argon flows, which bring about different pressures. **Bottom**: For a constant argon flow and two discharge currents, bracketing the one in the top figure. Arrows to the right and left indicate the branches for increasing and decreasing nitrogen flows, respectively. The dotted vertical line at $Q_N = 16$ sccm marks the approximate position of the stoichiometry point for $I = 5$ A.

These considerations enable us to draw a few conclusions: Firstly, the sputtering process can be characterized well by stepping the reactive-gas flow through an appropriate range and recording the stabilized target voltage at each flow value. Secondly, the working point of the process – at least in the zirconium-nitride system – is determined by the sputter current and by the nitrogen flow. This finding is contrary to the assumptions in some of the applied literature [25, 27] where relevance is given to the nitrogen–versus–argon flow ratio. (We were at first fooled into the latter assumptions ourselves, considering the flow ratio in Paper I and Paper i, so I hope to set the record straight with Paper II and this thesis.) Thirdly, since the erosion rate determines the amount of nitrogen needed to maintain a certain degree of compounding and itself is primarily determined by the discharge current, the reactive sputtering process is most easily performed in constant-current mode. Constant-power mode, where the voltage and hence the current may change for instance due to shutter movement, would probably require controlling the nitrogen gas flow depending on the momentary current.

Table 4.1: Controlled and resulting process parameters for the samples **I–IV** in Paper II. Q_N and Q_{Ar} are the nitrogen and argon flows, p is the mean process pressure, U is the mean target voltage and $\Delta d/\Delta t$ is the film-deposition rate (computed from the film thickness in Table 4.2 and the process duration).

Sample	Q_N	Q_{Ar}	p	U	$\Delta d/\Delta t$
	[sccm]	[sccm]	[mTorr]	[V]	[nm/s]
I	4	97	3.30	232	2.2
II	8	95	3.32	252	1.4
III	20	87	2.88	261	0.7
IV	36	76	3.00	273	0.5

Table 4.2: Some relevant properties of the Zr–N samples: d is the film thickness, a is the crystal-lattice constant (calculated from the precise peak positions in $\theta/2\theta$-XRD measurements), N/Zr describes the average atomic ratio of nitrogen to zirconium as obtained by ERDA, and ρ is the electrical resistivity; 'colour' is simply a subjective impression assessed by eye.

Sample	d	a	N/Zr	ρ	colour
	nm	[Å]		[$\mu\Omega$ cm]	
I	400	—	0.22	200	silver
II	250	4.60	1.07	100	golden
III	120	4.63	1.20	450	dark golden
IV	100	4.66	1.37	3000	grey-brown

4.2. Sputtered ZrN Films

Table 4.1 shows process parameters of the samples that are discussed in Paper II. Along with a process duration of 180 s and a sputter current of $I = 3$ A, which all four preparations shared, the nitrogen and argon flows were controlled parameters, while the chamber pressure, target voltage and deposition rate arose as a result of the target state and of the total amount of gas. At the sputter current used, the working point for stoichiometric ZrN was at a N flow of 8 sccm according to the investigation presented in the previous section. The sputtered films were analysed by profilometer, ERDA and grazing-incidence and $\theta/2\theta$-XRD as well as in terms of optical reflectance and electrical resistivity. Many of the film properties are summarized in Table 4.2, the GI-XRD diffractograms are plotted in Figure 4.2), and Figure 4.3 shows the reflectances in air as well as those calculated for a CIGS–reflector interface.

Our findings are as follows:

Sample I While the sample was deposited with a nitrogen flow that was half the calculated optimal working point, ERDA data points to material that contains only a fifth to a quarter of the amount of nitrogen needed for
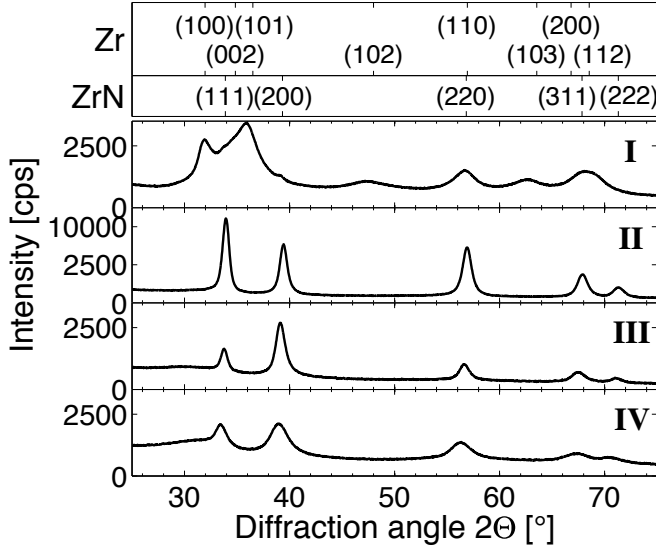
Figure 4.2: Grazing-incidence XRD patterns. The two topmost boxes list the positions of the relevant Zr and ZrN reflections; the Roman numbers in the main figure correspond to the samples listed in Tables 4.1 and 4.2.

stoichiometry, and the XRD diffractogram has broad and partly merged peaks that hint at a mixture of metallic Zr and ZrN of poor crystallinity. A resistivity higher than both in the pure metal and in sample **II** may be due to interstitial nitrogen that hinders the transport of electrons. The simulated reflectance at an interface to CIGS (using the method described in Section 3.2) shows no advantage over molybdenum in the interesting long-wavelength regime.

Sample II All analyses support the prediction that a nitrogen flow of 8 sccm is the optimal working point and show that the film is stoichiometric ZrN: According to ERDA, the N/Zr ratio is close to unity. XRD measurements shows only clear, strong peaks of the cubic ZrN phase and a ZrN lattice constant that is smallest among the three samples where it could be determined and closest to the literature value of cubic phase of 4.577 Å (PDF 35–0753 of the JCPDS-ICDD). Both the narrow XRD peaks (suggesting good crystallinity), the small lattice constant and the low resistivity imply that the crystal contains little interstitial nitrogen.

In absolute terms, a resistivity of $100\,\mu\Omega$ cm means our ZrN is more resistive than molybdenum (for which we typically see values around $10\,\mu\Omega$ cm), but it compares favourably with our doped zinc-oxide window, which has a resistivity another order of magnitude higher than ZrN. Thus, even if one were to use ZrN as a rear contact on its own,
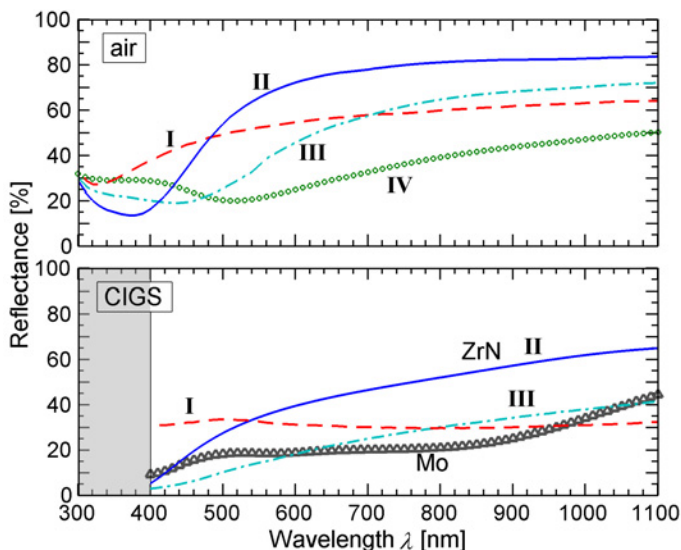
Figure 4.3: **Top**: Specular reflectance at near-normal incidence, as measured in air. **Bottom**: Simulated reflectance at several ZrN/CIGS interfaces, compared to a standard Mo/CIGS interface.

with a similar thickness as the typical Mo and ZnO:Al films (in the half-micrometre range), it would still be the window, and not the rear contact, that would be the "bottleneck" determining the minimal series resistance.

For the use at the interface to CIGS, the simulation predicts a significant increase of the reflectance to over 50 % for wavelengths above 750 nm, around or more than twice the corresponding values of molybdenum.

Sample III This sample, though sputtered with a considerably higher nitrogen flow than the one before, contains moderately more nitrogen according to ERDA. It shows the same XRD peaks, but they are broadened. This effect, and above all the increasing resistivity and the larger calculated lattice constant, can all be taken as an indication of an increasing amount of interstitial N that stretches the affected ZrN unit cells (not by very much, as the N atom is small compared to the Zr atom or ion, but measurably), as I argue with reference to Benia and co-workers [4].

Sample IV For this sample, the N/Zr ratio of about 4/3 shown by ERDA and the high resistivity suggest that the film probably consists to a good part of Zr_3N_4, and judging by the high background in the XRD diffractogram, this part of the film is presumably amorphous.

Further experiments have indicated that similarly high long-wavelength reflectances as at the voltage-peak point can be achieved in a reasonably large process window several sccm in nitrogen flow across. There is mostly room for variation towards higher nitrogen flows, as one can easily understand when considering that in the above experiments, the variation in flow between samples **I** and **II** changes the film's nitrogen content by a factor of close to 5, while the step to **III**, which is three times as wide, only adds another 10 % of nitrogen to the film.

Mechanical stress.

We have observed that the film stress correlates with the discharge current. The films prepared with a current of 3 A are reliably stable and well-adherent even now, after several years, while higher currents increasingly induced compressive stress, which over a time of minutes to months lead to cracks and flaking. The occurrence of compressive stress at higher currents may be connected to one or both of two effects: Firstly, higher currents lead to a higher growth rate, which can impede the relaxation of stress during growth; and secondly, high ion energies tend to lead to compressive stress, and low ion energies, to tensile stress, with a neutral zone in between [64]. Other than via the current, the ion energy could also be influenced by changing the pressure in the vacuum chamber (either by means of the argon flow or via the pumping speed): By causing more collisions between gas particles, higher pressure will act to reduce the ion energy, and the reverse is true for lower pressure.

It should be noted that all the given current, voltage and gas-flow values are thoroughly specific to the situation in our system and not easily scaled to another setup. The method presented in Section 4.1.2 should make it fairly straight-forward to find the correct relation between the sputter current and the nitrogen flow for reaching stoichiometric ZrN; other parameters such as the best settings for minimal stress will require some more experimentation.

4.3. CIGS Coevaporation

4.3.1. The BAK

All my absorber films have been produced in a *Balzers BAK 550* vacuum chamber ("the BAK") which is pumped by a cryo pump to base pressures that typically lie below 2×10^{-6} mbar. For each run, three $5 \times 5 \, cm^2$ substrates are mounted side by side on a sample holder made of graphite. The holder is then placed upside down beneath an array of quartz lamps, which serves to heat the graphite, and thus the samples, during the process.

Some 50 cm below and separated by a movable shutter, the open-boat sources for the metals are situated side by side, one each for Cu, In and Ga. A Se atmosphere is created during the process by evaporating Se from a

temperature-controlled crucible source that sits next to the metal sources and about 20 cm higher. In my processes, this selenium source is kept at a constant temperature, sufficiently high to assume that the Se evaporation rate is several times higher at all times during the process than the one required for the formation of stoichiometric material.

The metal sources are heated by current passing directly through them, and thanks to their small thermal mass they are quite fast-acting: Once hot, they can in principle go from no evaporation to 'full blast' in a few seconds, and back in just a little bit longer. This property offers the considerable advantage that one has great freedom in defining virtually any desired profile over time, from simple boxes (constant evaporation rates) to simulations of industry-scale in-line systems with hill-like profiles. The downside of the fast-acting sources is that neither regulating the powers directly nor controlling the source temperatures would work for controlling the evaporation rates in any reproducible manner. To solve this, the metal fluxes (rates) are instead observed by a quadrupole mass spectrometer (a *Balzers QMG 420* working with a secondary-electron multiplier) and the numbers are sent to a computer, which based on this feedback controls the power to each source so that the measured values reach their corresponding rate setpoint.

4.3.2. Old Baseline Recipe

Originally, the standard CIGS recipe in the BAK was one called the "Baseline". It is of a certain relevance here by virtue of having been used at the time of the ZrN investigations, in particular in Paper I. Its central process parameters are plotted in Figure 4.4.

General notes on process graphs.
Figures of this format, and excerpts of it, will return several times throughout the following sections. In the top graph, the rates of the three metals (copper, indium and gallium) are displayed with the axis on the left, and the substrate temperature, with the axis on the right. The rates are derived from mass-spectrometer data, scaled with XRF results (see Section 3.3.1) such that for each metal, the integral equals the atomic percentage multiplied with the film thickness. They are thus not real elemental rates but rather to be understood as 'partial film-growth rates'. The bottom graph visualizes the two compositional key parameters that I mentioned in Section 2.3 – the copper content CGI and the gallium content GGI. By default, as in this figure, both lines show the development of the *integral*, or average, contents of the whole film at each given point in time. As far as the copper content is concerned, that remains true in all cases; it is the relevant quantity here. As soon as we introduce grading between the evaporated gallium and indium, however, the main message that the average gallium content still conveys is to show that the final value is the same as that measured by XRF and thus prove that the calibration of the graph
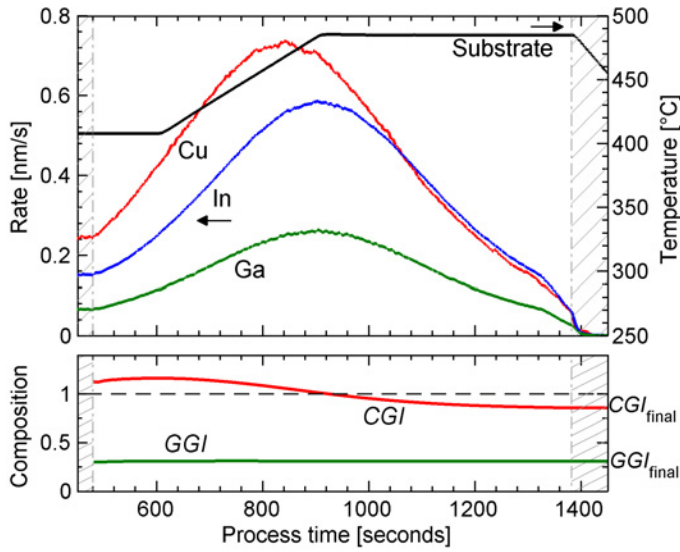
Figure 4.4: **Top**: Substrate temperature, and evaporation rates of the metals Cu, In and Ga of the original *"Baseline"* process as functions of process time. The rates are scaled data from the in-situ mass spectrometer. **Bottom**: Integrated composition in terms of the ratios GGI = $[\text{Ga}]/[\text{In}+\text{Ga}]$ and CGI = $[\text{Cu}]/[\text{In}+\text{Ga}]$. During segments displayed as shaded areas, a shutter is placed between the sources and the samples.

was correct. Instead, what becomes most relevant then is the *momentary* gallium content, the ratio of group-III elements arriving in the gas phase at each moment, because that can be directly compared to depth-profile analyses later on.

Specifics of the Baseline process.
Returning to the particular "Baseline" process shown in Figure 4.4, we can note two properties characteristic of this process: The first is the curved shape of the evaporation profiles in the upper graph, which are actually segments of cos^5 (cosine-to-the-power-of-five) functions and are meant to simulate the passage of a sample in front of static sources in an in-line system; and the second is the fact that the copper curve slightly precedes the group-III curves, leading to the Cu-rich-to-Cu-poor development visible in the lower graph. As in many coevaporation processes, the substrate temperature starts at a lower level, and is ramped up around the middle of the process.

4.3.3. The Family of Multi-Stage Recipes

As mentioned in Section 2.3, the class most interesting for devices is the one called *multi-stage processes*. In the rest of this thesis, I will use this term to designate all varieties of processes derived from the original *three-stage process* first presented by the NREL [12, 19]. These processes share the characteristic sequence beginning with the formation of $(In,Ga)_2Se_3$ by evaporation without any Cu (stage *I*), continuing with the evaporation of Cu to transform the film into $Cu(In,Ga)Se_2$ topped by Cu_2Se (stage *II*) and ending with the evaporation of In, Ga and Se (stage *III*) to consume the Cu_2Se and press the Cu content of the film below stoichiometry (CGI < 1). They are considered to become *multi*-staged if two of the fundamental stages overlap (as stages *II* and *III* do in Paper III) or if a stage is sub-divided into blocks with different element-flux ratios (as in Papers III, V and VI). In my nomenclature, I have retained the idea of the three-stage process, however, having the entirely Cu-free stages begin with the numerals '*I*' and '*III*' and the Cu-containing ones, with '*II*', respectively, and adding single lower-case letters to specify in detail, as for instance in 'stage *II.a*'.

Figure 4.5 shows the concrete implementation of the most straight-forward of the processes applied in this thesis (used in Papers V and VI). It is a pure three-stage process – that means, one without overlaps between stages – and a reference process, which means that the gallium and indium flux setpoints are in a constant relation to each other throughout the process, so that the metal fluxes do not introduce gradients to the ratio GGI = $[Ga]/[In+Ga]$ in the film. In the papers I called that kind of gradients 'intentional gradients', but here in the dissertation I would like to choose the term *extrinsic gradients* to contrast them with *intrinsic gradients*, which are gradients which the process may give rise to despite flat evaporation profiles.

The more general multi-stage variant, used in Paper III, is shown in Figure 4.6.

4.3.4. Chemical Reactions During CIGS Growth

To understand the development of gradients in CIGS, to be discussed in Section 4.4, it is useful to visualize the basic chemistry of the absorber growth. I will present it here separated into the reaction formulae for the various segments of a three-stage process, as it is the three-stage process at which I have looked closely. In other process types, the sequence of sample states will generally be different, some compositions may not even occur at all, but for a given composition, the reaction paths should certainly remain valid.
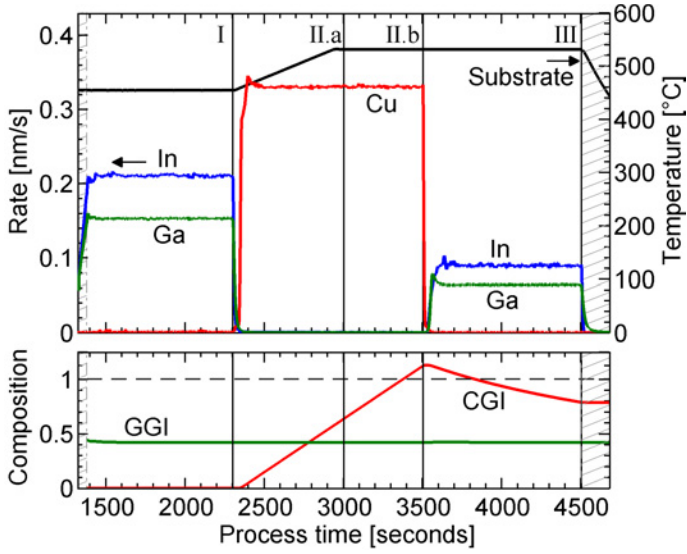
Figure 4.5: **Top**: Substrate temperature (scale on right-hand axis), and evaporation rates of the metals Cu, In and Ga (left-hand axis) of the pure *three*-stage reference process as functions of process time.
Bottom: Integrated gallium and copper contents. The symbols *I*, *II.a*, *II.b* and *III* indicate break-off points.
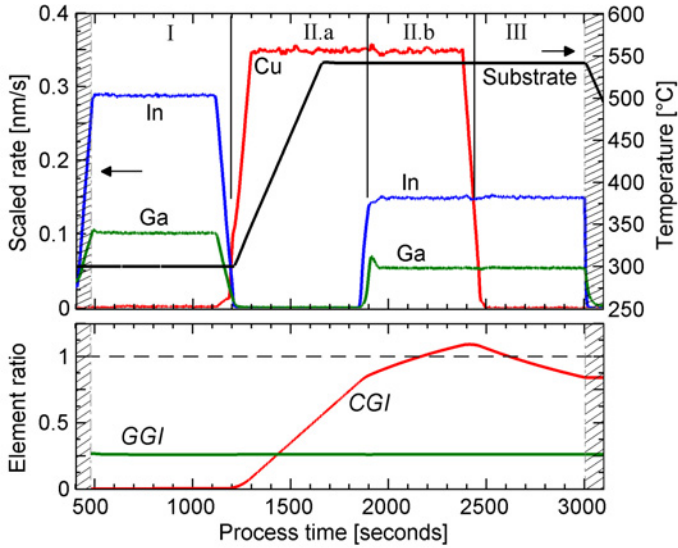
Figure 4.6: The same kind of profiles as in the figure above, but for the *multi*-stage reference process. Here, the symbols *I*, *II.a*, *II.b* and *III* indicate stages and partial stages.

35

Stage I:

To recapitulate, the three-stage CIGS process starts with a Cu-free 'precursor' $(In,Ga)_2Se_3$ formed from In, Ga and Se. The reaction is thus quite simply:

$$2\,(In,Ga) + 3\,Se \quad \rightarrow \quad (In,Ga)_2Se_3.$$
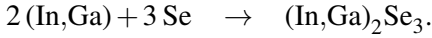
Stage II.1 (defect chalcopyrite):

In the second stage, Cu and Se are evaporated instead. The Cu diffuses into the film and finally reconstructs it into $Cu(In,Ga)Se_2$, but with the Cu arriving gradually, of course, there is not enough Cu available at first to form a complete CIGS film all at once. There are several *defect chalcopyrite* phases known, and these will form as long as little Cu is present relative to In and Ga. They constitute very Cu-poor variants of the CIGS phase where missing Cu is accounted for by means of point defects such as Cu vacancies and In_{Cu} and Ga_{Cu} anti-sites [10]. Among them are $Cu(In,Ga)_5Se_8$ ('1–5–8') and $Cu(In,Ga)_3Se_5$ ('1–3–5') [17], the latter also known by the name *ordered vacancy compound* (OVC) [55]. Let us consider the formation of $Cu(In,Ga)_3Se_5$ – the situation is analogous with other defect compounds – and treat the bulk and the growth surface separately:

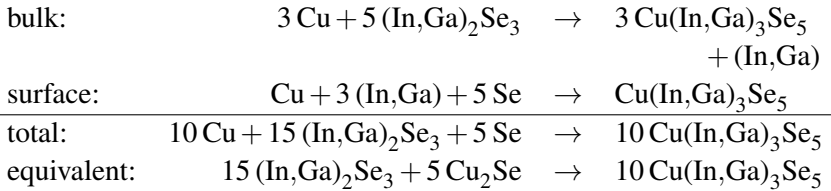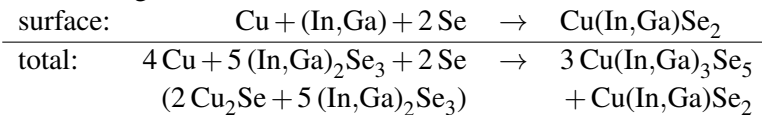|			
bulk:	$3\,Cu + 5\,(In,Ga)_2Se_3$	$\rightarrow$	$3\,Cu(In,Ga)_3Se_5$
			$+\,(In,Ga)$
surface:	$Cu + 3\,(In,Ga) + 5\,Se$	$\rightarrow$	$Cu(In,Ga)_3Se_5$
total:	$10\,Cu + 15\,(In,Ga)_2Se_3 + 5\,Se$	$\rightarrow$	$10\,Cu(In,Ga)_3Se_5$
equivalent:	$15\,(In,Ga)_2Se_3 + 5\,Cu_2Se$	$\rightarrow$	$10\,Cu(In,Ga)_3Se_5$

As one can see, for every three Cu atoms being built into the existing bulk, one In or Ga atom has to be removed in order to reach the correct sum formula. One can also view this constraint as "movement on the pseudo-binary tie line" or realize that it means charge balance: Cu has a valence of +1, the group-III atoms have a valence of +3, so in order to end up with the correct number of electrons, moving from one electrically neutral crystal structure to the other, one In or Ga atom has to make place for three Cu atoms. At the film surface, these group-III atoms have the opportunity to react directly with Cu and Se that arrive in the gas phase and form new chalcopyrite unit cells.

In the above block of formulae I have assumed that they continue to form the defect chalcopyrite, since one usually does not observe any Cu gradients in depth profiles of Cu-poor films. However, as an alternative route it is also possible that full CIGS unit cells form and Cu then simply diffuses onwards from them. This alternative would change the total numbers a bit but would not affect the general situation:

surface:	$Cu + (In,Ga) + 2\,Se$	$\rightarrow$	$Cu(In,Ga)Se_2$
total:	$4\,Cu + 5\,(In,Ga)_2Se_3 + 2\,Se$	$\rightarrow$	$3\,Cu(In,Ga)_3Se_5$
	$(2\,Cu_2Se + 5\,(In,Ga)_2Se_3)$		$+\,Cu(In,Ga)Se_2$

Stage II.2 (chalcopyrite up to stoichiometry):

Once enough Cu is present in the film, growth continues with Cu supplementing $Cu(In,Ga)_3Se_5$ to form proper $Cu(In,Ga)Se_2$ with a shrinking number of defects:

bulk:	$3\,Cu + 2\,Cu(In,Ga)_3Se_5$	$\rightarrow$	$5\,Cu(In,Ga)Se_2$
			$+\,(In,Ga)$
surface:	$Cu + (In,Ga) + 2\,Se$	$\rightarrow$	$Cu(In,Ga)Se_2$
total:	$4\,Cu + 2\,Cu(In,Ga)_3Se_5 + 2\,Se$	$\rightarrow$	$6\,Cu(In,Ga)Se_2$
equivalent:	$3\,(In,Ga)_2Se_3 + 3\,Cu_2Se$	$\rightarrow$	$6\,Cu(In,Ga)Se_2$
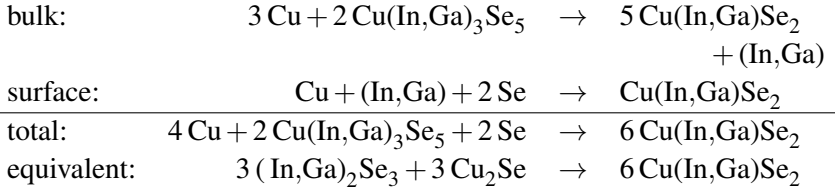
We can now see that it is not necessary to differentiate between the growth of the defect chalcopyrite and the growth of the chalcopyrite, since any point on the pseudo-binary tie line actually can be viewed as a "linear combination" of $(In,Ga)_2Se_3$ and Cu_2Se, CIGS being the result of one part of either. In extension, this fact implies two noteworthy things: (1) *Whenever* Cu diffuses into a film of Cu-poor chalcopyrite (or precur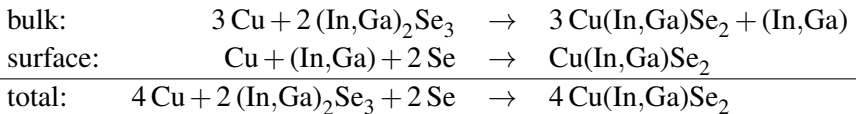sor), one group-III atom is expelled for each three Cu atoms; and (2) throughout the Cu-poor growth phase, the Se consumption is fixed in relation to the metal rate ($Se/M = 1/2$). The latter can be useful to know when estimating the necessary minimum Se flux of a process in the light of the findings of Wallin and co-workers [63], for example. (The same ratio is three times higher in stage I, $Se/M = 3/2$ – once again the atoms' different valence is clearly seen.) Conclusion (1) contradicts the assumption of Gabor et al. [19] who say that group-III counter-diffusion only begins once more Cu is added to a film of the composition $Cu(In,Ga)_3Se_5$. I will consider in Section 4.4.2 one factor that might make the profiles look as if no counter-diffusion occurred before that point in the process.

Stage II.1+2 (Cu-poor chalcopyrite):

In summary, the two preceding 'sub-stages' can be consolidated into one as follows:

bulk:	$3\,Cu + 2\,(In,Ga)_2Se_3$	$\rightarrow$	$3\,Cu(In,Ga)Se_2 + (In,Ga)$
surface:	$Cu + (In,Ga) + 2\,Se$	$\rightarrow$	$Cu(In,Ga)Se_2$
total:	$4\,Cu + 2\,(In,Ga)_2Se_3 + 2\,Se$	$\rightarrow$	$4\,Cu(In,Ga)Se_2$

Stage II.3 (Cu-rich sample, Cu being added):

When $Cu(In,Ga)Se_2$ stoichiometry is reached, practically all copper sites are filled and there is no room for additional copper in the crystal lattice. Instead, a copper-selenide phase (considered to be moderately Cu-deficient Cu_2Se, hence sometimes expressed as $Cu_{2-x}Se$) segregates at the surface and at grain boundaries [54,60], of which we also found evidence – by GI-XRD and SIMS – in Paper VI:

surface:	$2\,Cu + Se$	$\rightarrow$	Cu_2Se
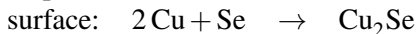
Tuttle and co-workers [60] postulated that given a Se overpressure, the copper-selenide layer might transform into CuSe which could be liquid at

sample temperatures above 523 °C. This liquid film might be acting as a flux-ing agent, which is considered to be the reason why a Cu-rich stage pro-motes the formation of large CIGS grains. However, the results of Rau and Rabenau [47] seem to indicate that at normal CIGS process temperatures and pressures, $Cu_{2-x}Se$ is the only stable phase. This observation is also supported by the more recent work of Kim [32], and the film's melting point in this case would probably be 1115 °C [47], far outside the CIGS process window. Even so, Cu_2Se might facilitate the transition towards larger CIGS grains by filling voids between grains and offering diffusion paths between them.

Stage III.1 (Cu-rich sample, In and Ga being added):

After a layer of Cu_2Se has been grown for a while, In and Ga are reintro-duced. The general reaction occurring is obviously the following, consuming the Cu_2Se film as long as is present:

$$Cu_2Se + 2\,(In,Ga) + 3\,Se \quad \rightarrow \quad 2\,Cu(In,Ga)Se_2$$

The only question is *where* the reaction takes place. One might imagine that the new atoms chemically react with the very surface upon arrival at the sample, maybe drawing Cu from the Cu_2Se layer below. However, in micro-scopic cross-sections of absorbers one generally does not observe widespread discontinuities of the crystal at a corresponding depth in the film. That obser-vation implies strongly that the new CIGS unit cells grow epitaxially at the surface of the CIGS film after the necessary reagents have diffused through the Cu_2Se layer. In this case, the reagents are buffered in the Cu_2Se film and thus do not have to react directly from the gas phase. Independent of whether that film is liquid or solid, this fact might enhance the epitaxial growth.

Stage III.2 (Cu-poor):

Finally, when the Cu_2Se layer has been consumed, CIGS formation contin-ues at the surface by virtue of Cu out-diffusion from the existing CIGS film, reducing the bulk Cu content once more to below 1.

$$Cu + (In,Ga) + 2\,Se \quad \rightarrow \quad Cu(In,Ga)Se_2$$

Again, precisely as in Stage II.1+2 above, it holds that in order to maintain the charge balance, the movement of three Cu atoms (here their removal from the existing CIGS bulk and addition to the newly growing material) has to be compensated for by an opposite movement of one In or Ga atom.

4.4. Gradients in Multi-Stage Absorbers

This section is about the development of Ga gradients in CIGS absorbers grown in multi-stage processes (both with and without overlaps between stages *II* and *III*). In Paper III, we showed that one can maintain extrinsic gradients both at the front and close to the back contact, and then dealt with the electrical effects of such gradients, which I will discuss in Section 5.2.

Since there had been a fairly wide-spread conception that the in-diffusion of Cu and the ensuing Cu-rich phase in the second stage caused major In–Ga interdiffusion and would mostly flatten gradients other than the famous 'notch' of three-stage CIGS, my findings about the gradients raised the question anew how gradients (extrinsic *and* intrinsic ones) actually develop over the course of a multi-stage process. This question became the subject matter of Paper VI, and with the findings from this paper a few additional conclusions can also be drawn from Paper III. I will in the following explain my understanding of the development first of the 'intrinsic' gradients (that is, what is commonly known as the 'notch') and then of the 'extrinsic' gradients.

4.4.1. Intrinsic Gallium Gradients

In Paper VI, I investigated two series of four CIGS samples each, prepared with the overlap-free three-stage process where evaporation was broken off at different points in the process. The series relevant in this section is the *reference* series with no variation in the ratio between the Ga and In evaporation rates. I illustrated the process earlier in Figure 4.5 (page 35). As marked in the figure, one evaporation run was discontinued at the end of the first stage (symbol *I*), one in the middle of the second stage (*II.a*), one at the end of the second stage (*II.b*), and one not at all (*III*), yielding a complete absorber film.
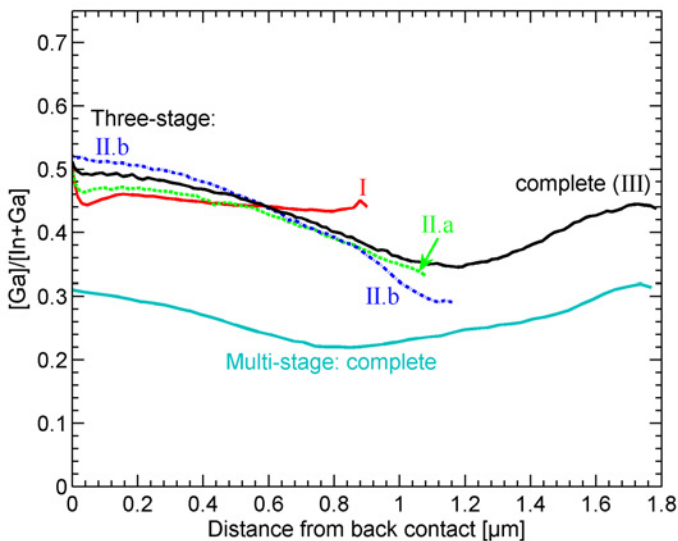

Figure 4.7: SIMS GGI depth profiles of all reference (intrinsically graded) samples from Papers III (three-stage) and VI (multi-stage), plotted as functions of the distance from the back surface. The Roman numbers refer to the break-off points marked in Figure 4.5.

The group of lines captioned 'Three-stage' in Figure 4.7 – and marked with the same symbols – shows the $[Ga]/[In+Ga]$ depth profiles determined by SIMS from the corresponding samples. One sees clearly that In and Ga are still as evenly distributed as evaporated at the end of the first stage, but that a strong forward gradient has developed by the middle of stage *II* (point *II.a*) and apparently continues to grow during the remainder of stage *II*, and that another, reverse gradient forms on top of the earlier one during stage *III*, by which it completes the well-known 'notch' profile that one expects in multi-stage processes.

In the paper, I assert that this gradient development can be explained well by the need for charge compensation during Cu movement, when combined with the hypothesis that the diffusivity of Ga in the film is lower than that of In: If all diffusion of Cu in CIGS has to be accompanied by contrary movement of group-III elements, as I have elaborated in Section 4.3.4, and if Ga moves slower than In, then the inward diffusion of Cu in stage *II* will cause preferential movement of In to the front, and conversely, the outward diffusion of Cu in stage *III* will cause preferential movement of In away from the front.

Indeed, it is not only conjecture from the direction of the gradients that implies a lower diffusivity of Ga, but Nishwaki and co-workers [43] come to the same conclusion. We also find a separate piece of evidence ourselves, in the CGI profiles of the samples aborted after the Cu-poor first half of stage *II* (point *II.a*) in Figure 4.8: In the extrinsically graded sample (which has more Ga at the back than the reference), the CGI profile slopes downward towards the back, while the copper seems evenly distributed in the reference case. This difference suggests that it is a lower mobility of the gallium that hinders the movement of copper in the sample containing more gallium.

During the Cu-rich part of the third stage, an additional gradient-forming effect may be the epitaxial growth of CIGS on the Ga-depleted surface grown in the second stage, where it is conceivable that lattice matching would initially favour the inclusion of In into the new CIGS, leading to Ga accumulating in the Cu_2Se film, which in turn gradually would shift the equilibrium so that more Ga would then be included. I do have to note, though, that this part *is* only conjecture on my part; it might be a worthwhile future experiment also to abort growth at a point during the early, Cu-rich stage *III*.

Influence of stage lengths and the overlap.
To conclude this section about intrinsic gradients, I want to compare the SIMS profiles of the two complete samples in Figure 4.7, the multi-stage sample being the reference from Paper III (the process was illustrated in Figure 4.6). I think that the relevant differences between these two specific processes are the following: (1) In the multi-stage process, the ratio between the amount of group-III elements evaporated before and during/after the addition of Cu is approximately 1/1; in the three-stage process, this ratio is about 2.5/1. (2) In the multi-stage process, stages *II* and *III* overlap, while in the three-stage pro-

cess they do not. (3) The multi-stage process starts with a considerably lower substrate temperature than the three-stage process (see Figures 4.5 and 4.6), although it reaches the same temperature in stage *II*.

It seems safe to say that as a result mainly of the first difference, the position of the gradient minimum ('notch') shifts so that the first gradient spans approximately the material grown during stage *I* and later converted to CIGS, and that the relation between the maximum gradient levels at the back and at the front also correlates with the ratio between the amounts of material in the group-III stages.

Nakada and co-workers [41] have found a clear temperature dependence of the magnitude of intrinsic gradients in CIGS films grown in a three-stage process on (Na-free) metal foil, with more interdiffusion at higher temperatures. I will return to the question of the temperature dependence of the interdiffusion in the following section, but for now I want to note again that the two processes discussed above have the same substrate temperature after about the first quarter of stage *II*, and that the GGI profiles are not expected to deviate from a homogeneous distribution during stage *I*, where the temperature differs most. I would therefore argue that the different initial temperatures should have no significant impact on the intrinsic gradients that this section concerned.

4.4.2. Extrinsic Gallium Gradients

Preparation.

Extrinsic Ga gradients were investigated in three papers, numbers III, V and VI. The recipe variations used to achieve the gradients are summarized as GGI profiles in Figure 4.8.

In Paper III, the material-science aim was to test to which degree extrinsic gradients would still be present after a multi-stage process. In order to try and introduce a back-surface field, more Ga was evaporated at the beginning of the first stage (stage *I.a*) and less Ga was evaporated in the remainder (top left in Figure 4.8). By this it was ensured that the average of GGI at the end of stage *I* was the same as in the reference, excluding the possibility that any observed gradients were the result of different Ga contents during the Cu-rich stage. As we will see, here it also played a significant role that the substrate temperature in stage *I* was lower in this process than in the others (see again Figures 4.5 and 4.6). Ga-rich layers of varied thickness (varied relative duration) were also introduced at the interface-side end of some absorbers (top right).

In Paper V, nominally Ga-free $CuInSe_2$ top layers were achieved by turning off the Ga source near the end of the third stage (bottom left in Figure 4.8).

With the second series of samples in Paper VI (lower right in Figure 4.8), we investigated the *development* of an extrinsic gradients at the back, starting evaporation with a thin layer only containing Ga at the back (GGI = 1), that
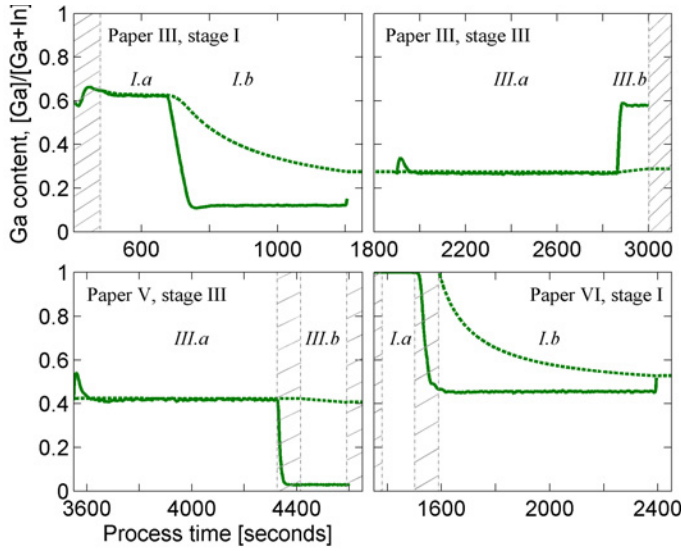
Figure 4.8: The evaporation profiles used to induce the different extrinsic gallium gradients in this thesis, expressed as the momentary GGI ratio (solid lines) and the average (integrated) GGI ratio (dashed lines). **Top left**: Stage-*I* profile for the back-surface field Paper III. **Top right**: Stage-*III* profile for widening the bandgap at the interface (the relative duration of the Ga-rich stage was varied). **Bottom left**: Stage-*III* profile for the In-enhanced top layers in Paper V (showing the case for the thickest top layer). **Bottom right**: Stage-*I* profile for the extrinsic gradient in Paper VI.

was concluded by a step to the same Ga content as in the reference series (GGI ≈ 0.45).

Results and Discussion.

The main results are summarized in the form of SIMS depth profiles for Paper III in Figure 4.9, and for Papers V and VI in Figure 4.10.

In the SIMS profiles from Paper III we see that it is absolutely possible in principle to achieve a fairly pronounced extrinsic gradient at the back of a CIGS film grown in a multi-stage process, a gradient that is affected only by a moderate degree of interdiffusion. As the data from that paper and from Paper V illustrate, less surprisingly, a moderate degree of interdiffusion applies also to either kind of extrinsic gradients (Ga-rich or In-rich) at the top of the CIGS films. All gradients are reduced in their magnitude and correspondingly spread out over a greater depth relative to how they were evaporated, but they nevertheless remain reasonably strong and localized. For instance, in Paper V, an evaporated 100 nm thick film of $CuInSe_2$ yields an affected thickness of ca. 200 nm to 300 nm with a GGI value reduced by roughly a third relative to the reference.
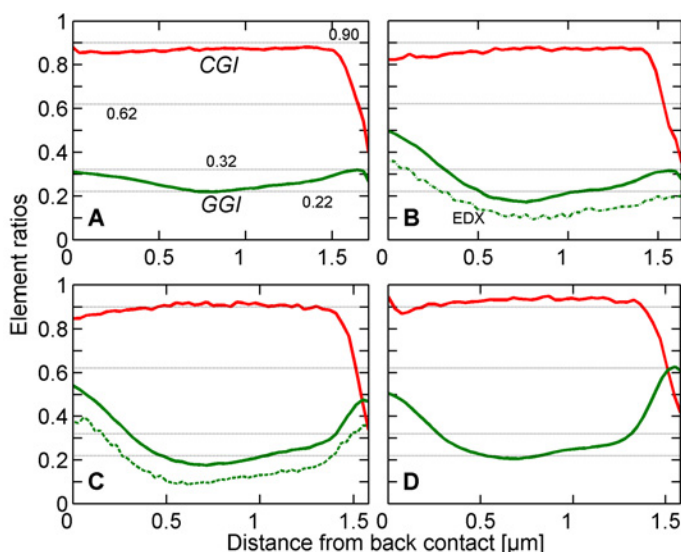
Figure 4.9: SIMS composition profiles of all films from Paper III, displayed as the ratios $[Ga]/[In+Ga]$ and $[Cu]/[In+Ga]$ over the distance from the back surface. The letters in the box corners refer to the samples in the paper: **A**: Reference as in Figure 4.6. **B**: With a gradient in the back, as shown in Figure 4.8 (top left). **C**: Additionally with a gradient in the front, as shown in Figure 4.8 (top right). **D**: Ditto, but the evaporation for the front gradient was just over twice as long as in case C.

However, the SIMS data in Paper VI demonstrate that a localized back-side gradient can by no means be taken for granted. They also show clearly that the critical interdiffusion occurs not during the Cu-rich segment of the process (as was assumed by Gabor and co-workers [19] and others) but, quite to the contrary, during the Cu-*free* stage *I* and the Cu-poor beginning of stage *II*. As Lundberg and co-workers [40] showed that In–Ga interdiffusion is stronger in Cu-rich CIGS if it is free of Na, though, the irrelevance of the Cu-rich stage to interdiffusion might strictly speaking only be true in the presence of Na, as is the case in my experiments, which were performed on sodium-containing glass without a barrier.

Combining the findings from Paper III and Paper VI, it is obvious that the In–Ga interdiffusion in those stages is relatively slow at the lower substrate temperature of 300 °C but quite fast at 450 °C. Since the substrate temperatures from stage *II* onwards are identical in both series and other process parameters such as the process length and the maximum Cu excess are largely the same as well, the survival of the back-side gradient in Paper III shows that interdiffusion decreases considerably, even at the high final substrate temperature in our processes, once the most Cu-deficient stages are passed. Evidence
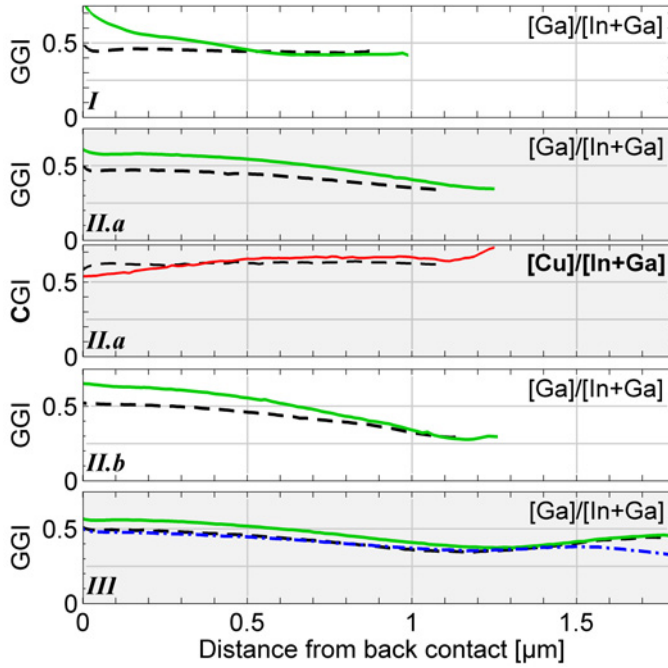
Figure 4.10: SIMS composition profiles of all films from Paper VI, displayed as the ratio $[Ga]/[In+Ga]$ over the distance from the back surface – for the point *II.a* also in terms of $[Cu]/[In+Ga]$. The Roman numbers in the box corners again refer to the break-off points marked in Figure 4.5. Solid lines are from the intentionally graded samples; dashed lines are from the references (the same data as in Figure 4.7). In the bottom figure, a dash-dotted line shows furthermore the profile with the thickest In-rich top layer in Paper V.

published by Chirila and co-workers [11] supports the conclusion that less interdiffusion occurs in later stages.

The threshold for the decrease of the interdiffusion rate most probably lies at approximately $CGI = 1/3$ (in other words, around the composition of the defect compound $Cu(In,Ga)_3Se_5$), as Caballero and co-workers [10] indicate after finding no extrinsic gradients left in material that hardly exceeded $CGI = 0.35$ during growth, citing a higher Ga mobility due to a high concentration of V_{Cu} defects as the probable reason for the strong interdiffusion.

5. CIGS Devices

In the previous chapter, I have covered all the processing techniques I have been concerned with, presenting in particular how to find the proper working point of a reactive sputter process and some properties of ZrN films fabricated by such a process, and discussing CIGS recipes and the development of gradients during the CIGS growth. With that, it is now time to look at the application in solar-cell devices of the ZrN films and gradients examined in the previous chapter, summarizing the electrical findings of Papers I, III and V.

In this chapter we shall consider the electrical results of a number of devices, starting with a discussion of how devices less than a micrometre thick might benefit from a ZrN back reflector and then looking at the effect of various gradients on normally thick devices and also how a process should be designed to achieve them.

5.1. Application of ZrN in Thin CIGS Devices

In Paper I, we trialled the use of ZrN back reflectors in $0.5\,\mu m$ thick CIGS solar cells.

A first challenge was that ZrN proved to be a diffusion barrier for sodium, but tends to contain pinholes, where it does not block off Na. That property is problematic since the CIGS seems locally to attract Na all the stronger at the pinholes: With Na having a considerable lateral diffusion length in CIGS [7], the pinholes cause high Na concentrations in the CIGS over them and in the vicinity. There the Na obviously forms one or more water-soluble compounds (visible as lighter patches on an otherwise dark-grey CIGS surface), and while we do not have any thorough understanding of these compounds, we have often observed that they cause detachment of CIGS in the CBD process. We were able to suppress this problem by supplying Na evenly to the complete sample area in the form of a Na-containing NaF precursor layer. The precursors provided a homogeneous overall Na concentration that was presumably beneficial for the electronic properties of the film but also prevented excessive local Na clustering.

Figure 5.1 illustrates the three structures **A** through **C** that we examined in Paper I, and the electrical results are listed in Table 5.1. We found that a direct ZrN/CIGS contact (sample **A**), yielded rather poor cells having both a high electron recombination rate (seen as a large saturation-current density

and a high ideality factor in the diode model) and a high series resistance, which we interpreted as the effect of a hole barrier (downward-bending of the valence band) at the back contact. We therefore investigated two alternative approaches to passivate the rear contact: Ga grading at the back of the absorber (Figure 5.1 B), and a very thin $MoSe_2$ (molybdenum-selenide) film grown from a sacrificial, ca. 10 nm thick Mo layer deposited on top of the ZrN (Figure 5.1 C). The motivation for the latter is that a $MoSe_2$ layer usually forms on its own by the interaction of Se with the Mo contact in the beginning of the CIGS growth and that the layer is attributed with passivating the back contact [50], but that it cannot form in the basic sample due to the ZrN layer.
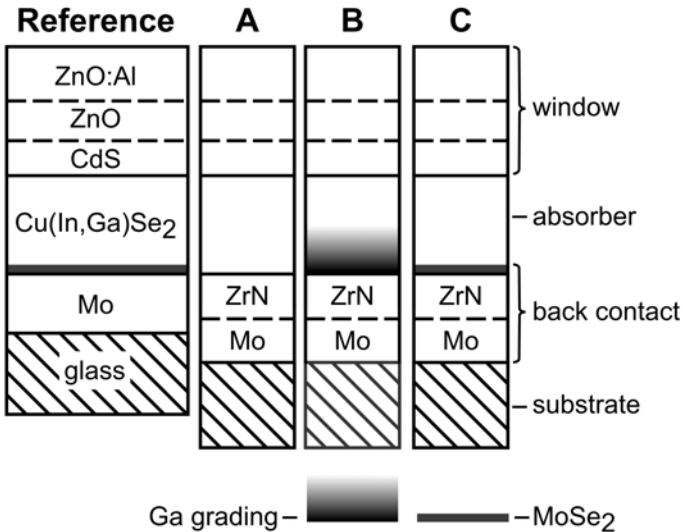
Figure 5.1: Standard structure of a CIGS solar cell and modified structure of the ZrN rear-reflector samples investigated. A: direct ZrN, B: with Ga grading, and C: with $MoSe_2$ contact layer.

We see that the grading in sample **B** reduces the recombination losses in the ZrN sample, but still leaves a high series resistance in place. The finding firstly shows that the ZrN/CIGS contact was poorly passivated for electrons in the basic case, probably presenting as much as a downward-banding conduction band edge at the interface, but that the passivation can be improved considerably by overriding the disadvantageous band bending with the increase of the conduction-band edge that a sufficiently strong Ga gradient causes. Secondly, the finding affirms the assumption that the resistance is caused by a hole barrier at the contact, for since the Ga concentration only affects the conduction band, one would not expect the gradient to change the situation for holes.

Sample **C** was intended to address both problems together by introducing a band structure approximately like that suggested by Rau and Schock [50] via a ZrN/$MoSe_2$/CIGS interface, and Table 5.1 demonstrates that this ap-

Table 5.1: Firstly, the *average* AM 1.5 solar-cell parameters of the cells of the ZrN reflector devices (in brackets: Mo reference devices) in runs **A**–**C**: Open-circuit voltage (V_{OC}), fill factor (*FF*), short-circuit current density (J_{SC}) and power-conversion efficiency (η). V_{OC} and *FF* values are obtained directly from JV characteristics, while J_{SC} and η values are calculated using QE spectra. Secondly, the one-diode model parameters obtained from a fit to the JV characteristics of the *best* cells Diode saturation current density (J_0), ideality factor (n_{id}), series resistance (R_S) and shunt conductivity (G_{sh}).

	Run:	A	B	C
V_{OC}	[mV]	456 (535)	572 (637)	580 (518)
FF	[%]	62.8 (72.5)	66.0 (70.9)	70.5 (69.8)
J_{SC}	[mA/cm^2]	24.9 (25.0)	26.9 (25.5)	25.4 (25.5)
η	[%]	7.2 (9.7)	10.2 (11.4)	10.4 (9.2)
J_0	[mA/cm^2]	3.0×10^{-4}	8.0×10^{-5}	1.9×10^{-6}
		(4.1×10^{-6})	(5.3×10^{-6})	(9.0×10^{-6})
n_{id}	[-]	1.6 (1.4)	1.8 (1.6)	1.4 (1.4)
R_S	[$\Omega\,$cm^2]	0.94 (0.60)	0.84 (0.35)	0.69 (0.64)
G_{sh}	[mS/cm^2]	4.3 (1.3)	1.4 (1.0)	2.3 (2.2)

proach is fairly successful, reducing recombination by more than another order of magnitude and reducing the series resistance to a level comparable to the references, thereby improving all of the solar-cell parameters and yielding an average efficiency higher than in the reference devices. Unfortunately, the short-circuit current density on this sample is slightly *worse* than on the corresponding reference. However, while one might think that this effect is caused by reduced reflectance at the back due to the additional MoSe$_2$ layer, optical measurements carried out on devices (shown in Paper I) show that the reflectance indeed is still improved by the ZrN reflector and that it instead is the collection of carrier pairs generated by long wavelengths that is reduced relative to the reference. A plausible reason for this shortcoming is the fact that control problems during the NaF deposition for this run had caused a much higher Na supply to the ZrN sample than intended, which through the doping effect of Na probably reduced the depletion-zone width so far that the collection from the lowest part of the absorber suffered.

Thus, I would still assert that adding a very thin Mo film on top of the reflector is a well-functioning way to passivate the back interface in a ZrN-reflector sample. Additionally applying a rather localized Ga gradient may be the optimal solution for minimizing the loss of electrons at the back contact.

As we discussed later on in Paper IV, given the present cost structure for PV modules, a technique that causes an efficiency loss is not tolerable economically if it does not cut the production by at least an equal amount. On the one

hand, then, a ZrN back-contact reflector has the ability to compensate some absorption losses and thus to allow for thinner films that can be produced with less material consumption and higher plant throughput. On the other hand, we were not able to boost the efficiency of sub-micrometre devices to the level of today's thick devices by using ZrN, and it would add complexity to today's production by requiring reactive sputtering and a separate Na supply. In the light of Paper IV ZrN does not seem viable for production today. Nonetheless, changing circumstances such as rising In prices might still offer new fields of application for ZrN in the future, and I hope to have presented some useful findings here that can be built upon.

5.2. Effects of Enhanced Gradients

5.2.1. Gallium-enhanced Back Side

Both in Papers III and VI, we found gains in V_{OC} and *FF* (and consequently in η) when we added Ga gradients at the back of the absorbers, which largely corroborates the general assumption that back-side fields are beneficial. JV curves from Paper III are shown in Figure 5.2.

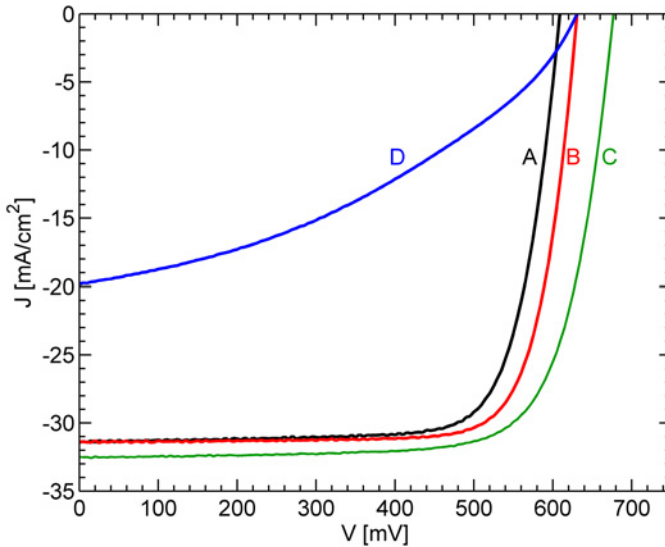*Figure 5.2:* Illuminated JV curves of cells from the samples in Paper III, with actual gradients as shown in Figure 4.9.

In the simulations in Paper V we found indications that our material probably has diffusion lengths in the order of 0.6 μm, fairly small compared to the absorber thickness. Based on the discussion at the end of Section 2.1, one might therefore expect a greater gain from the more spread-out gradient in

Paper VI than from the more localized one in Paper III, but the reverse is true. It should be kept in mind, though, that the final gradient in Paper VI was actually quite weak. Furthermore, the different overall gallium content in the two series and the somewhat dissimilar shape of the intrinsic gradients may both have affected the sensitivity of the resulting devices to extrinsic gradients.

However, I think that the main benefit of my studies in this respect is to offer new design rules for ensuring that one's multi-staged process yields the desired back-side gradient.

In general, as discussed before, if the absorber thickness is similar to the diffusion length, one will want a sharp, localized gradient, especially if minimizing absorption losses (in a sub-micrometre absorber) is another design goal besides contact passivation. For this case, my findings show that it really is important to keep the initial substrate temperature in the range of $300\,^\circ$C or below, and furthermore that it probably is wise only to ramp the temperature up around the middle of the second stage, when the Cu content has exceeded $30\,\%$ to $40\,\%$. It seems that an extended Cu-rich stage does not increase the interdiffusion of gradients, and taking into account conclusions from the literature, the only scenario where it might interfere with the gradient design would be if there were no Na present.

A low initial substrate temperature should work well even with an absorber that is thick compared to its electron-diffusion length, since a more extended gradient can always be achieved by spreading the extrinsic grading over a wider distance.

5.2.2. Gallium-enhanced Front Side

In Paper III we also tested the effect of an increase of the Ga content towards the CIGS/CdS interface. As demonstrated in Figure 5.2, we managed to achieve a further respectable increase of V_{OC} with a moderate gradient of this sort (sample **C**). It is a bit uncertain whether the increase seen in J_{SC} is an actual effect of the gradient (possibly by an extended space-charge region because of the higher bandgap at the front) or whether it depended on other uncontrolled process variations. However, already this JV curve has a *FF* that is somewhat reduced relative to the reference and the sample with the back-surface gradient, and going on to the wider and stronger gradient in sample **D**, one sees quite how devastating a badly controlled front-side gradient could be for device performance. This JV curve is a brilliant example of the effect of the voltage-dependent photo-current collection that I mentioned in Section 2.1: The dark JV curve (shown in Paper III) shows that no particular shunt is present, but the light JV curve here has a strong slope throughout, causing an abysmal fill factor and, what is more, even reducing the short-circuit current density severely.

Figure 5.3 illustrates the reason for this behaviour with a device, simulated in SCAPS, where we emulated the front-side gradient of sample **D** with a
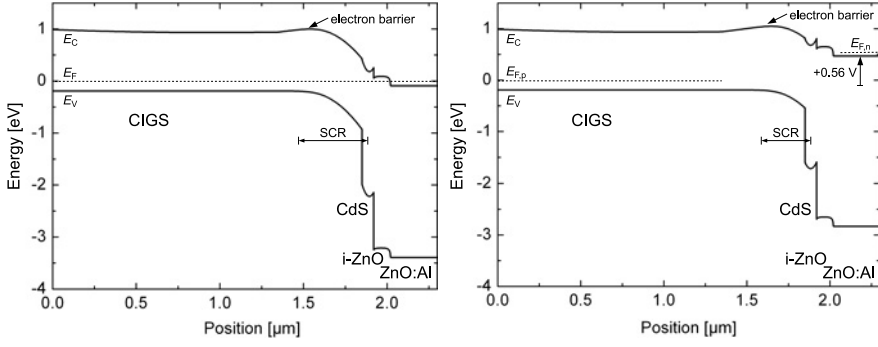
Figure 5.3: Two energy-band diagrams (simulated by SCAPS) of a CIGS device that has intrinsic Ga grading and at the interface additionally a linear gradient towards GGI = 0.6 spanning over 0.5 μm. **Left**: At equilibrium (no bias voltage). **Right**: At the maximum-power point ($V = 0.56$ V). (Diagrams courtesy of Jonas Pettersson.)

500 nm wide linear slope rising to GGI = 0.6 at the front, and which shows a similar JV behaviour. The figure shows the energy-band diagram at the short-circuit point and at the maximum-power point, and it is clearly visible how the gradient gives rise a considerable 'hill' in the conduction band. This hill constitutes a barrier for electrons that ought to transit from the absorber to the window, and it becomes all the higher at forward bias, where the space-charge region is gradually reduced both in width and height. The fill-factor reduction in sample **C** is undoubtedly the same effect, only with a gradient that is small enough to be overridden by the steep slope of the space-charge region for most voltages up to around the maximum-power point.

To conclude this section, gallium enhancement at the front – certainly enhancement going beyond the soft slope of a typical intrinsic gradient – runs a high risk of causing worse electrical performance.

5.2.3. Indium-enhanced Front Side

Finally, we investigated in Paper V the scenario of an extrinsically *reduced* Ga content (enhanced In content) in a thin layer at the very front of the absorber, as it was suggested by Repins and co-workers [51].

I mentioned already briefly in Section 4.4.2 that the Ga-free layers that we had evaporated turned out to have inter-diffused. As a matter of fact, with the thinnest top layer (as suggested in the NREL paper), the reduction of the surface Ga content was still within the margin of error of our XPS analysis.

The electrical results were fairly inconclusive, showing hardly any statistically significant improvement with nominal top-layer thicknesses between 20 nm and 100 nm, but on the up side, neither showing any deterioration at

all, although a small bandgap at the *p–n* junction would generally tend to lead to more recombination. The only potential exception from the lack of differences was an improvement of the fill factor in the devices with the thinnest top layer (nominally 20 nm) that was comparable to the improvement seen by the NREL, relative to the respective references.

Our electrical simulations with SCAPS showed that apart from a slight decrease of V_{OC} (compensated for by an increase of J_{SC}), no appreciable change of device characteristics should be expected up to a nominal top-layer thickness of 100 nm (which was simulated as a linear gradient spanning twice the nominal thickness). It was not possible at this stage to model additional features that might be beneficial, such as a more optimal lattice match between In-rich material and CdS or reduced oxidation of In relative to Ga.

In conclusion, although we have not found clear evidence for a considerable positive effect of an In-enhanced CIGS surface, I see it as a useful finding in itself that this modification proves not to be detrimental: After all, it can be hard in practice exactly to control the geometry and alignment of all the sources in an in-line deposition system, which means that unplanned gradients may occur in the films. For that reason, it is good to know to which extent such gradients can be tolerated without jeopardising device performance, and while the previous section has shown that a Ga-content rise in the top region is likely to emerge as a barrier for electrons under forward bias, the final results here indicate that a localized drop in the Ga content near the surface is uncritical.

6. Concluding Remarks

In this thesis I have discussed several issues which are more or less directly related to two possible approaches to making CIGS-based solar cells ever more competitive: Firstly, reducing their manufacturing costs, and secondly, increasing the power output per module (for what a customer is ultimately interested in is not the price per module, but the cost per kWh it generates).

By minimizing the CIGS thickness, both throughput costs and material costs can be reduced, but for these cost reductions to be economically relevant, it is necessary that the efficiency is maintained and that the modification does not add too much complexity to the production technology. We were able to show a beneficial optical effect of a ZrN back reflector and we could demonstrate ways to mitigate the back-contact problems that we encountered. In the process we found that the shortcomings were related to electron losses and a hole barrier at the back contact, which could be alleviated by means of a very thin sacrificial Mo layer that forms a passivating film of $MoSe_2$ and optionally by an additional Ga gradient that further keeps electrons away from the back contact.

ZrN films were fabricated by reactive sputtering in a nitrogen-containing atmosphere. We achieved films with good resistivity, good adhesion, and optimal reflectance in the region of interest, namely the near-infrared part of the spectrum. I have also presented a method that allows relatively quickly to find the sputtering parameters that lead to these desired properties in a given sputter system.

In the other part of the thesis, the focus was on the three-stage process, which is known for yielding solar cells with high efficiencies. In Paper VI, we presented a model for how the Ga profile develops during the three stages, and the model was further discussed in the thesis. We have shown that we can enhance the profiling by adding more or less Ga in relation to In in different stages of the process and that these "extrinsic" gradients were smoothed to some extent but could still be found in the finished CIGS film, particularly when the initial substrate temperature was not too high.

The electrical effect of the Ga profiles was investigated by characterization of solar-cell devices, with support from electrical modelling using SCAPS. In the work concerning band-gap engineering of the surface of the CIGS films, we found that a thin layer of Ga-free CIGS at the surface hardly improved the solar-cell efficiencies but neither harmed them, but that an excessive Ga concentration at the CIGS surface could be devastating for device performance.

In the future, the need for using less In may lead to a revisit of the "thin" CIGS strategy. ZrN is a promising candidate for a reflecting back contact and has conductivity enough to act a as sole back contact without an underlying Mo layer. In addition, it acts as a diffusion barrier to Na, a fact that may prove useful for controlling the Na content in finished CIGS films.

The three-stage process is in heavy use by research labs around the world and has yielded small-area cells with highest efficiencies, but it has not yet made it to large scale production. It is my belief that the results from the research presented here will help in understanding how to optimize and control this process and possibly increase efficiency also at the module level.

A. BAK Upgrade

Around the middle of my term, I contributed major parts, especially the software, to a joint campaign to modernize the process-control system of the BAK.

Old system.

The original control system dated back to the early 1980s and was built around a dinosaur of a *JET 80* computer interfacing to – some – hardware components on the machine through a custom-built electronics box. Major disadvantages of this old system, besides the risk of failure in obsolete and ageing 25-years-old components, were the computer's insularity (inability to connect to a modern network), its meagre processing power (the processor's clock rate being 4 MHz) and its minuscule disk capacity (two 5.25" floppy-disk drives being the only storage devices). Due to these factors, the computer was only able to store and interpret fixed-size binary 'recipe' (instruction) files to control the metals, the substrate heater and the shutter. The selenium source had to be set by hand via a separate *Eurotherm* controller, virtually all configuration of the mass spectrometer had to be done by hand, and, most severely, data could only be logged permanently by means of an analogue plotter that could record at most four parameters (usually the metal rates were chosen, and additionally the substrate power or the mass-spectrometer reading of water). What is more, with the computer lacking a proper real-time clock, the duration of process runs was notoriously imprecise, often deviating upward or downward from the nominal full hour by several minutes.

New system.

In contrast, we have based the new control system on a modern yet lean desktop computer with a Linux operating system. High computer reliability is aimed for by running in 'headless mode' without direct user input, instead communicating with the user remotely through its Ethernet network connection, and by using a processor that does not need a cooling fan thanks to operating at a reduced clock rate (500 MHz). Serial ports connect the computer to the mass spectrometer – which was retained from the old setup –, to the *Eurotherm* temperature controllers for the substrate and the selenium source, and to the *Optomux* electronics components governing the metal sources and the shutter. Power output is sent from the electronics to sources and heaters by means of the same bank of thyristors as before, albeit through rerouted and

much tidied-up data and power cables. Also the vacuum-control system was retained, but tidied up.

Software.

The new software toolbox provides a number of interactive text-mode interfaces and command-line utilities (all written as object-oriented *FreePascal* code) as well as a web interface (written in *PHP*) for plotting process variables and a *MATLAB* class for analysing and plotting process logs.

eva.

At the core of the toolbox is the program for controlling the process, 'eva'. It delegates the control of the temperature-controlled heaters (substrate and selenium source) to their own *Eurotherm* controllers, but implements itself full proportional–integral–derivative (PID) controllers for the rate-controlled sources and besides that manipulates the shutter as well as a power-controlled 'auxiliary' source which can be used for evaporating an additional substance such as NaF. In its normal operation mode, the program follows the instructions given to it in a human-readable recipe file, a text file with tabulator-separated columns where each row stands for a process step and each column represents for instance the process time, the shutter state, or the power or setpoint for a particular source.

While executing a recipe, the operator can step in at any time by entering commands on a program-internal command line to pause, restart or abort the process, set a source to a new (constant) setpoint, reset it to follow the recipe once again, or change its PID control parameters. The program can also be started in manual mode by not providing a recipe-file name. These possibilities for manual control are invaluable for troubleshooting and for trialling new settings.

During a process, the control program writes twenty-four values to a log file for the current process at least once a second. Recorded values include the shutter state, the setpoints, actual values and powers of all sources and heaters, and the pressures in the main chamber, the mass-spectrometer cavity and the cryo pump.

pro.

Recipe files can be edited in another of the provided programs, '*pro*', which offers visual aids, such as highlighting of steps where the shutter is open, and commands for multiplying, adding to and ramping whole or partial columns. As the recipes are plain text files, the operator has also the option to edit them in any text editor or in a spreadsheet program such as Excel.

Old system: Reproducibility.

The old system's recipe files were restricted to twenty process steps, which were easily used up to define the soft curves of the then-baseline recipe (see

Figure 4.4). It therefore used to be the routine manually to set and activate the selenium source (which had to be done anyway) and the substrate heater for their joint quarter-hour pre-heating period and to stand by with an alarm clock to execute the recipe after the correct time, the recipe then beginning with the metal sources' additional warm-up period. This added the human factor to the mix and decreased the reproducibility of the process timing, as did the need to be present to switch off the selenium source precisely at the end of the evaporation, both adding to the problem already given by the old computer's varying process speed.

New system: Reproducibility.

In the new system, thanks to the unrestricted number of steps in the new recipes, the reliable precision of the process timing guided by the PC's real-time clock, and thanks to all actuators in the process control – shutter, sources and heaters – being under the full control of the computer, it is possible not only reproducibly to pinpoint the duration of the evaporation to a second, but also to define a *complete* process in the recipe, extending the precision of the timing to the whole duration from the beginning of the pre-heating period to the end of the evaporation. At the same time, this also ensures that all parameters are logged during both the pre-heating period and the complete cool-down period after the evaporation, which is of considerable value both for verifying whether two process runs are comparable to each other and for investigating technical problems such as temporary pressure spikes or loose connections to sources.

Process-analysis software.

The most sophisticated analysis facilities for the new system are based on the environment for scientific computing *MATLAB*. From the MATLAB command window or a file dialogue, the user specifies a log file to be imported into a MATLAB data object, which reads the file and then automatically calibrates the rates, translating the 'raw' rates (mass-spectrometer readings) into actual partial growth rates according to the results of a XRF measurement (see Section 3.3.1). The XRF data are read directly from a database if they are available there for the given process. Alternatively, the calibration of a previous run can also be saved to a configuration file and retrieved later on, so that a rough quantitative examination of a run can be carried out even if XRF data are not yet available for it, as for instance when observing an ongoing process or trying out a simulation (see below). Once the log is imported, it is straight-forward to display a process synopsis listing among other values the final copper and gallium contents and film thickness, and to plot a tableau of graphs that includes, as functions of time, the temperatures, raw and calibrated metal rates, powers, pressures and the as-deposited composition profiles, and the latter also as functions of the growing film thickness. Another command

creates publication-ready graphs summarising the process, such as the one shown in Figures 4.4 through 4.6 and 4.8.

Simulator.

The *simulator* companion to the process-control program uses the same code as the latter to interpret a recipe, but instead of sending commands to the hardware in real time, it rapidly steps through the recipe in nominal one-second intervals and writes a log file where the setpoint values are inserted instead of measured values. This makes it possible to anticipate very quickly the outcome of a new or altered recipe, iterating through several adaptation cycles if needed and plotting the simulated results to verify setpoint-profile forms, shutter states and – given a valid, recent mass-spectrometer calibration – even estimated composition and thickness developments.

Sammanfattning på svenska

Reflekterande ZrN-kontakter och gallium-gradienter i Cu(In,Ga)Se$_2$-solceller

Bakgrund

Det sägs att "money makes the world go round" och det är kanske på sätt och vis sant, men om man tänker efter är nog energi ännu viktigare för att vårt moderna samhälle och ekonomin ska fungera. Enligt Internationella Energiorganet IEA var jordens energiförbrukning år 2008 hela 8428 megaton kolekvivalenter (Mtoe), eller 100 PWh (100 billioner kWh), av vilka 17,2 % var i form av elektricitet.

Det finns en hel del problem med de tekniker för energiomvandling som används idag: Fossila bränslen såsom kol och olja kommer på sikt att bli allt svårare att komma åt och bidrar dessutom till växthuseffekten, och i Japan har man nyss sett tydligt hur svårt det är att hantera kärnklyvning på ett säkert sätt.

Å andra sidan är effekten hos solljuset en solig dag på vår planet ungefär $1000\,W/m^2$. Om man räknar efter lite grann så ser man att den energi som varje minut når den sida av jorden som vetter mot solen motsvarar världens totala energikonsumtion för tre hela dagar. Det finns alltså solenergi i överflöd, det gäller bara att ta den tillvara! Solceller är ett av flera sätt att göra det.

Solceller omvandlar solljus direkt till elektricitet, är tysta och under användning helt koldioxidfria. De är också mycket stabila – man räknar med att en solcellsmodul har en livslängd på över 20 år. I tider där både klimat och energianvändning diskuteras är solceller aktuellare än någonsin, och de är den form av förnybar energiomvandling som växer snabbast med en femtioprocentig ökning av installerad effekt under 2010. En stor del av förklaringen till ökningen i installationer står att finna i stödsystem som införts i en rad länder, bland annat i Tyskland. Med den ökade produktionsskalan och med den ökade konkurrensen på en växande marknad sjunker nu priserna på solcellsmoduler snabbt och målet är att behovet av stöd snart ska kunna upphöra. Den hårdnande konkurrensen kräver att gränserna för vad som är tekniskt möjligt att uppnå avseende verkningsgrad och tillverkningskostnad ständigt pressas på alla nivåer.

Den här avhandlingen behandlar forskning på metoder som är tänkbara för att sänka kostanden för tillverkning av solceller. Den första viktiga komponenten är att teknologin som används är tunnfilmssolceller där det aktiva materialet är mycket tunt och belagt på en vanlig glasskiva. Avhandlingen diskuterar

dessutom sätt att ytterligare minska kostnaderna för denna typ av solceller. Tekniken bygger på halvledarmaterialet Cu(In,Ga)Se$_2$ (CIGS), som har mycket hög ljusabsorberande förmåga och därför kan göras tunt. CIGS-solceller är uppbyggda av en bakkontakt, normalt av metallen molybden, ett CIGS-skikt, ett buffertskikt och en transparent ledande framkontakt, som efter varandra beläggs på en skiva av fönsterglas. Jag har använt bufferskikt av CdS och odopad ZnO, samt ZnO-skikt dopade med aluminium som ledande framkontakt. CIGS-skiktet har tillverkats genom vakuumförångning, där koppar, indium, gallium och selen förångas samtidigt och reagerar med varandra på den molybdenbelagda glasskivan, där de bildar kristallkorn. Uppbyggnaden av en CIGS-solcell visas schematiskt i figur 1 ("Reference").
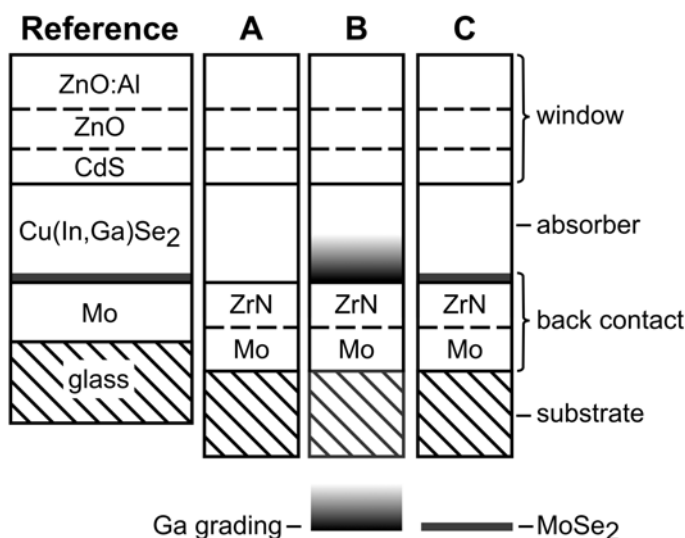
Figur 1: De olika teststrukturer som användes för att testa ZrN som optisk reflektor. Längst till vänster referensen som är den struktur som vi normalt använder, där ett skikt med MoSe$_2$ bildats spontant och verkar som en kontaktförbättring, sedan följer en struktur med enbart ZrN som inte alls fungerar bra, ZrN med ökad gallium vid bakkontakten, där det ökade galliuminnehållet verkar som en barriär för elektroner (mer om detta beskrivs nedan), samt slutligen en struktur med ZrN kombinerat med ett MoSe$_2$-skikt.

Optiskt reflekterande bakkontakter med ZrN

I den första delen av avhandlingen diskuteras hur man med bibehållen absorption kan minska tjockleken för CIGS-skiktet i tunnfilmssolcellerna, genom att använda en bakkontakt som reflekterar ljus. Det ljus som inte absorberas på en gång reflekteras vid bakkontakten och kan få en andra chans. Materialet som använts som reflektor är zirkoniumnitrid (ZrN). ZrN har en gyllene färg och är dessutom mycket hård. Skikten tillverkades med reaktiv sputtering och vi va-

rierade sputterinställningarna för att få de rätta proportionerna för en optimalt reflekterande film i det våglängdsområde som är mest intressant, nämligen den nära infraröda delen av ljusspektrum. Vi visade också på ökad absorption i mätningar på färdiga solceller. Nackdelen med ZrN är att det inte ger en god elektrisk kontakt till CIGS-skiktet. Därför har flera olika skikt utprovats för att få en förbättrad kontakt. En bild som beskriver de skikt som testats visas i figur 1. Genom att öka galliumhalten mot ZrN fick vi en viss förbättring. Genom att lägga till ett ultratunt Mo-skikt som sedan seleniserades till $MoSe_2$ fick vi också en viss gynnsam effekt.

Slutsatserna från denna del av avhandlingen var att det var svårt att helt undvika att verkningsgraden försämrades när CIGS-skiktet tunnades ner, trots de åtgärder som vidtogs och att det därför inte skulle vara lönsamt i produktion med tanke på den ökade komplexiteten detta skulle innebära.

Gallium-gradienter i CIGS-skikt

Den andra delen av avhandlingen handlar om hur man optimerar bandgap som funktion av djupet i CIGS-filmen. CIGS har egenskapen att det går att variera bandgapet genom att variera proportionerna mellan indium och gallium. Elektroner som rör sig i solcellen kommer att påverkas av bandgapsförändringar och man kan på så vis bland annat hindra elektroner från att rekombinera vid bakkontakten och därmed ökar sannolikheten för att de når *p–n*-övergången.

Den process som använts i denna del bygger på den så kallade trestegsprocessen, som hittills lett till de högsta verkningsgraderna för celler av CIGS. Det är en process där man alternerar förångning av indium, gallium och selen med förångning av koppar och selen i tre steg. Förångningen beskrivs mer i detalj i figur 2. Trots att indium och gallium som synes förångas i konstanta proportioner relativt varandra kommer de att variera i förhållande till varandra i den färdiga filmen. Hur detta går till och hur man kan påverka gallium-indium-profilen har varit fokus för mitt arbete under de senaste åren. Jag presenterar en modell för detta i avhandlingen.

Förutom de spontant bildade gallium-indium-profilerna har jag också arbetat med att förstärka och förändra dessa genom att till exempel förånga delar av CIGS-skikten helt utan gallium eller indium, eller med andra proportioner än referensen under delar av processen, men kompenserat upp till "rätt" grupp-III-förångning. I till exempel fallet med indiumfri förångning har därför mängden gallium ökats för att motsvara gallium+indium i referensprocessen.

Vissa av dessa förändringar har indikerat förbättringar i cellprestanda och ökad verkningsgrad, men vi har också visat att man ska vara mycket försiktig med för höga galliumkoncentrationer mot ytan av CIGS-skiktet, eftersom det kan leda till att elektronerna blockeras. Följden blir då en mycket låg ström och därmed låg verkningsgrad.
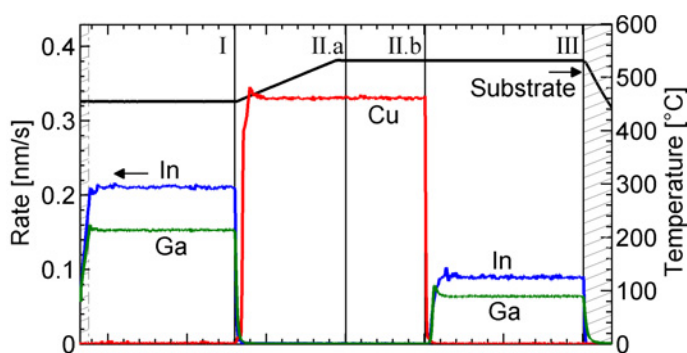
Figur 2: Trestegsprocessen. Bilden visar förångningshastighet (rate) för de olika metallerna som funktion av tid. Selen förångades i överskott under hela förångningen.

Sammanfattning

Sammanfattningsvis har avhandlingen inneburit att förståelsen för vad som händer med framför allt indium och gallium under CIGS-förångningen ökat. Jag har visat på potentiella möjligheter att förbättra prestanda för celler med mycket tunna CIGS-skikt med hjälp av optiska reflektorskikt i kombination med strategier för att förbättra de elektriska egenskaperna vid bakkontakten. Jag har också bidragit till att utveckla en sputterprocess för högreflekterande ZrN med goda egenskaper, såsom hög vidhäftningsförmåga och god reflektans i det nära infraröda området.

Acronyms

CBD chemical bath deposition. 23, 45
CBO conduction-band offset. 11

EDX energy-dispersive X-ray spectroscopy. 18, 19
ERDA elastic recoil detection analysis. 21, 28–30
    ToF-E ERDA Time-of-flight elastic recoil detection analysis. 21
ESCA electron spectroscopy for chemical analysis. 17

JV current-density–voltage analysis. 13, 14, 47–50

PID proportional–integral–derivative. 56

QE quantum-efficiency analysis. 14, 15, 47

SDL surface-defect layer. 8, 11
SEM scanning electron microscopy. 18
SIMS secondary-ion mass spectrometry. 18–21, 37, 40, 42, 43

TEM transmission-electron microscopy. 8, 9, 18, 19

XPS X-ray photoelectron spectrometry. 17, 50
XRD X-ray diffraction. 17, 29, 30
    $\theta/2\theta$**-XRD** $\theta/2\theta$ X-ray diffraction. 17, 28
    GI-XRD Grazing-incidence X-ray diffraction. 17, 28, 37
XRF X-ray fluorescence. 16, 18, 19, 32, 57

Bibliography

[1] María Isabel Alonso, Miquel Garriga, Carlos Alberto Durante Rincón, Elvis Hernández, and Máximo León (2002). 'Optical functions of chalcopyrite $CuGa_xIn_{1-x}Se_2$ alloys'. *Applied Physics A: Materials Science & Processing* **74**, pp. 659–664. doi:10.1007/s003390100931.

[2] American Society for Testing and Materials (ASTM) (2003). 'Reference Solar Spectral Irradiance: Air Mass 1.5'. URL http://rredc.nrel.gov/solar/spectra/am1.5/.

[3] Bülent M. Başol, Vijay K. Kapur, Arvind Halani, Craig R. Leidholm, Jon Sharp, James R. Sites, Amy Swartzlander, Richard Matson, and Harin Ullal (1996). '$Cu(In,Ga)Se_2$ thin films and solar cells prepared by selenization of metallic precursors'. *Journal of Vacuum Science & Technology A: Vacuum, Surfaces, and Films* **14** (4), pp. 2251–2256. doi:10.1116/1.580056.

[4] Hadj Mohamed Benia, M. Guemmaz, Guy Schmerber, Aimé Mosser, and Jean Claude Parlebas (2002). 'Investigations on non-stoichiometric zirconium nitrides'. *Applied Surface Science* **200**, pp. 231–238. doi:10.1016/s0169-4332(02)00925-x.

[5] Hadj Mohamed Benia, M. Guemmaz, Guy Schmerber, Aimé Mosser, and Jean Claude Parlebas (2004). 'Optical and electrical properties of sputtered ZrN compounds'. *Catalysis Today* **89** (3), pp. 307–312. doi:10.1016/j.cattod.2003.12.006.

[6] Sören Berg and Tomas Nyberg (2005). 'Fundamental understanding and modeling of reactive sputtering processes'. *Thin Solid Films* **476** (2), pp. 215–230. doi:10.1016/j.tsf.2004.10.051.

[7] Marika Bodegård, Lars Stolt, and Jonas Hedström, 'The influence of Na on the grain structure of $CuInSe_2$ films for photovoltaic applications'. In 'Proceedings of the 12th European Photovoltaic Solar Energy Conference, Amsterdam', pp. 1743–1746 (1994).

[8] Marc Burgelman and Jonas Marlein, 'Analysis of graded band gap solar cells with SCAPS'. In 'Proceedings of the 23rd European Photovoltaic Solar Energy Conference', p. 2151 (2008).

[9] Marc Burgelman, Peter Nollet, and Stefaan Degrave (2000). 'Modelling polycrystalline semiconductor solar cells'. *Thin Solid Films* **361–362**, pp. 527–532. doi:10.1016/S0040-6090(99)00825-1.

[10] Raquel Caballero, Víctor Izquierdo-Roca, Xavier Fontané, Christian A. Kaufmann, Jacobo Álvarez García, Axel Eicke, Lorenzo Calvo-Barrio, Alejandro Pérez-Rodríguez, Hans-Werner Schock, and Joan Ramón Morante (2010). 'Cu deficiency in multi-stage co-evaporated $Cu(In,Ga)Se_2$ for solar cells applications: Microstructure and Ga in-depth alloying'. *Acta Materialia* **58** (9), pp. 3468–3476. doi:10.1016/j.actamat.2010.02.021.

[11] Adrian Chirila, Dominik Guettler, David Brémaud, Steffen Bücheler, Raineesh Verma, Sieghard Seyrling, Shiro Nishiwaki, S. Haenni, Gerhard Bilger, and Ayodhya Nath Tiwari, 'CIGS solar cells grown by a three-stage process with different evaporation rates'. In '34th IEEE Photovoltaic Specialists Conference', pp. 000812–000816 (2009). doi:10.1109/PVSC.2009.5411161.

[12] Miguel A. Contreras, John R. Tuttle, Andrew M. Gabor, Andrew L. Tennant, Kannan Ramanathan, Sally E. Asher, Amy Franz, James C. Keane, L. Wang, John Scofield, and Rommel Noufi, 'High-Efficiency $Cu(ln,Ga)Se_2$-based Solar Cells: Processing of Novel Absorber Structures'. In '24th IEEE Photovoltaic Specialists Conference', pp. 68–75 (1994). URL http://www.oberlin.edu/physics/Scofield/pdf_files/pvsc-95h.pdf.

[13] Thorsten Dullweber, Olle Lundberg, Jonas Malmström, Marika Bodegård, Lars Stolt, Uwe Rau, Hans-Werner Schock, and Jürgen H. Werner (2001). 'Back surface band gap gradings in $Cu(In,Ga)Se_2$ solar cells'. *Thin Solid Films* **387** (1–2), pp. 11–13. doi:10.1016/s0040-6090(00)01726-0.

[14] Marika Edoff. Personal communication.

[15] Murat Eron and Allen Rothwarf (1984). 'Effects of a voltage-dependent light-generated current on solar cell measurements: $CuInSe_2/Cd(Zn)S$'. *Applied Physics Letters* **44** (1), pp. 131–133. doi:10.1063/1.94577.

[16] Murat Eron and Allen Rothwarf (1985). 'Interface charging and solar-cell characteristics: $CuInSe_2/CdS$'. *Journal of Applied Physics* **57** (6), pp. 2275–2279. doi:10.1063/1.334375.

[17] Michael L. Fearheiley (1986). 'The phase relations in the Cu,In,Se system and the growth of $CuInSe_2$ single crystals'. *Solar Cells* **16**, pp. 91–100. doi:10.1016/0379-6787(86)90076-1.

[18] Andrew M. Gabor, John R. Tuttle, David S. Albin, Miguel A. Contreras, Rommel Noufi, and Allen M. Hermann (1994). 'High-efficiency $CuIn_xGa_{1-x}Se_2$ solar cells made from $(In_x,Ga_{1-x})_2Se_3$ precursor films'. *Applied Physics Letters* **65** (2), pp. 198–200. doi:10.1063/1.112670.

[19] Andrew M. Gabor, John R. Tuttle, Michael H. Bode, Amy Franz, Andrew L. Tennant, Miguel A. Contreras, Rommel Noufi, D. Garth Jensen, and Allen M. Hermann (1996). 'Band-gap engineering in $Cu(In,Ga)Se_2$ thin films grown from $(In,Ga)_2Se_3$ precursors'. *Solar Energy Materials and Solar Cells* **41–42**, pp. 247–260. doi:10.1016/0927-0248(95)00122-0.

66

[20] Hubert Gnaser (1994). 'Improved quantification in secondary-ion mass spectrometry detecting MCs^{+} molecular ions'. *Journal of Vacuum Science & Technology A: Vacuum, Surfaces, and Films* **12** (2), pp. 452–456. doi:10.1116/1.579262.

[21] Martin A. Green, *Solar Cells: Operating Principles, Technology and System Applications* (Prentice-Hall, 1998). ISBN 0 85823 580 3.

[22] Steven Hegedus and William N. Shafarman (2004). 'Thin-film solar cells: Device measurements and analysis'. *Progress in Photovoltaics: Research and Applications* **12** (2–3), pp. 155–176. doi:10.1002/pip.518.

[23] Charles H. Henry (1980). 'Limiting efficiencies of ideal single and multiple energy gap terrestrial solar cells'. *Journal of Applied Physics* **51** (8), pp. 4494–4500. doi:10.1063/1.328272.

[24] Christopher J. Hibberd, Elisabeth Chassaing, Wei Liu, David B. Mitzi, Daniel Lincot, and Ayodhya Nath Tiwari (2010). 'Non-vacuum methods for formation of Cu(In,Ga)(Se,S)$_2$ thin film photovoltaic absorbers'. *Progress in Photovoltaics: Research and Applications* **18** (6), pp. 434–452. doi:10.1002/pip.914.

[25] Lili Hu, Dejie Li, and Guojia Fang (2003). 'Influence of N$_2$:(N$_2$+Ar) flow ratio and substrate temperature on the properties of zirconium nitride films prepared by reactive dc magnetron sputtering'. *Applied Surface Science* **220**, pp. 367–371. doi:10.1016/s0169-4332(03)00843-2.

[26] Philip Jackson, Dimitrios Hariskos, Erwin Lotter, Stefan Paetel, Roland Wuerz, Richard Menner, Wiltraud Wischmann, and Michael Powalla (2011). 'New world record efficiency for Cu(In,Ga)Se$_2$ thin-film solar cells beyond 20 %'. *Progress in Photovoltaics: Research and Applications* doi:10.1002/pip.1078. Published online.

[27] Jiann-Shing Jeng, Shin-Hui Wang, and Jen-Sue Chen (2007). 'Effects of substrate bias and nitrogen flow ratio on the resistivity and crystal structure of reactively sputtered ZrN$_x$ films at elevated temperature'. *Journal of Vacuum Science & Technology A: Vacuum, Surfaces, and Films* **25** (4), pp. 651–658. doi:10.1116/1.2735966.

[28] Lars B. Jonsson, Tomas Nyberg, and Sören Berg (1999). 'Target compound layer formation during reactive sputtering'. *Journal of Vacuum Science and Technology A: Vacuum, Surfaces, and Films* **17**, p. 1827. doi:10.1116/1.581898.

[29] Stanislav Kadlec, Jindrich Musil, and Jiri Vyskocil (1987). 'Influence of the pumping speed on the hysteresis effect in the reactive sputtering of thin films'. *Vacuum* **37** (10), pp. 729–738. doi:10.1016/0042-207X(87)90262-4.

[30] Marc Kaelin, Dominik Rudmann, Fedor V. Kurdesau, Hans Zogg, Toby Meyer, and Ayodhya Nath Tiwari (2005). 'Low-cost CIGS solar cells by paste coating and selenization'. *Thin Solid Films* **480-481**, pp. 486–490. URL http://www.sciencedirect.com/science/article/B6TW0-4DXSRH5-8/2/b4df1d52ebb60dee8150452897cb4d1c.

[31] John Kessler, Dieter Schmid, R. Schaffler, and S. Menezes, 'Electro-optical and photoelectrochemical studies of $CuIn_3Se_5$ chalcopyrite films'. In '23rd IEEE Photovoltaic Specialists Conference', pp. 549–554 (1993).

[32] Woo Kyoung Kim (2006). *Study of Reaction Pathways and Kinetics in $Cu(In_xGa_{1-x})Se_2$ Thin Film Growth*. Ph.D. thesis, University of Florida. URL http://ufdc.ufl.edu/UFE0015717/00001.

[33] Claus F. Klingshirn, *Semiconductor Optics* (Springer, Berlin, 2005), 2 ed. doi:10.1007/b138175.

[34] Wei Li, Yun Sun, Wei Liu, and Lin Zhou (2006). 'Fabrication of $Cu(In,Ga)Se_2$ thin films solar cell by selenization process with Se vapor'. *Solar Energy* **80** (2), pp. 191–195. doi:10.1016/j.solener.2005.07.011.

[35] David R. Lide, *CRC Handbook of Chemistry and Physics* (CRC Press, Boca Raton, FL, 2007), 88 ed. URL http://www.hbcpnetbase.com/.

[36] Michael A. Lieberman and Allan J. Lichtenberg, *Principles of Plasma Discharges and Materials Processing* (Wiley Interscience, 2005), 2nd ed. ISBN 0-471-72001-1.

[37] Daniel Lincot, Jean-François Guillemoles, S. Taunier, D. Guimard, J. Sicx-Kurdi, A. Chaumont, O. Roussel, O. Ramdani, C. Hubert, J. P. Fauvarque, N. Bodereau, L. Parissi, P. Panheleux, P. Fanouillere, Negar Naghavi, P. P. Grand, M. Benfarah, P. Mogensen, and O. Kerrec (2004). 'Chalcopyrite thin film solar cells by electrodeposition'. *Solar Energy* **77** (6), pp. 725–737. doi:10.1016/j.solener.2004.05.024.

[38] Margareta Linnarsson. Personal communication.

[39] Margareta K. Linnarsson and Bengt G. Svensson (1999). 'Cascade mixing in $Al_xGa_{1-x}As/GaAs$ during sputter profiling by noble-gas ions'. *Physical Review B* **60** (20), pp. 14302–14310. doi:10.1103/PhysRevB.60.14302.

[40] Olle Lundberg, J. Lu, Angus Rockett, Marika Edoff, and Lars Stolt (2003). 'Diffusion of indium and gallium in $Cu(In,Ga)Se_2$ thin film solar cells'. *Journal of Physics and Chemistry of Solids* **64** (9-10), pp. 1499–1504. doi:10.1016/S0022-3697(03)00127-6.

[41] Tokio Nakada, Takeshi Yagioka, Kyohei Horiguchi, Taku Kuraishi, and Takahiro Mise, 'CIGS thin film solar cells on flexible foils'. In '24th European Photovoltaic Solar Energy Conference', p. 2425 (2009). Session Code 3DO.4.3.

[42] Alex Niemegeers, Marc Burgelman, and Alexis De Vos (1995). 'On the $CdS/CuInSe_2$ conduction band discontinuity'. *Applied Physics Letters* **67** (6), pp. 843–845. doi:10.1063/1.115523.

[43] Shiro Nishiwaki, Takuya Satoh, Yasuhiro Hashimoto, Takayuki Negami, and Takahiro Wada (2001). 'Preparation of $Cu(In,Ga)Se_2$ thin films at low substrate temperatures'. *Journal of Materials Research* **16** (2), pp. 394–399. doi:10.1557/JMR.2001.0059.

[44] Per Nostell, Arne Roos, and Daniel Rönnow (1999). 'Single-beam integrating sphere spectrophotometer for reflectance and transmittance measurements versus angle of incidence in the solar wavelength range on diffuse and specular samples'. *Review of Scientific Instruments* **70** (5), p. 2481. doi:10.1063/1.1149781.

[45] Kay Orgassa, Hans Werner Schock, and J. H. Werner (2003). 'Alternative back contact materials for thin film Cu(In,Ga)Se$_2$ solar cells'. *Thin Solid Films* **431–432**, pp. 387–391. doi:10.1016/S0040-6090(03)00257-8.

[46] Jonas Pettersson, Charlotte Platzer-Björkman, Uwe Zimmermann, and Marika Edoff (2011). 'Baseline model of graded-absorber Cu(In,Ga)Se$_2$ solar cells applied to cells with Zn$_{1-x}$Mg$_x$O buffer layers'. *Thin Solid Films* **In Press, Corrected Proof**. doi:10.1016/j.tsf.2010.12.141.

[47] Hans Rau and Albrecht Rabenau (1970). 'Vapour pressure measurements in the copper-selenium system'. *Journal of Solid State Chemistry* **1** (3–4), pp. 515–518. doi:10.1016/0022-4596(70)90135-0.

[48] Uwe Rau (2004). 'Electronic Properties of Cu(In, Ga)Se$_2$ Thin-Film Solar Cells – An Update'. *Advances in Solid State Physics* **44**, pp. 27–38. doi:10.1007/b95888.

[49] Uwe Rau and Hans-Werner Schock (1999). 'Electronic properties of Cu(In,Ga)Se$_2$ heterojunction solar cells – Recent achievements, current understanding, and future challenges'. *Applied Physics A (Materials Science Processing)* **A69** (2), pp. 131–47. doi:10.1007/s003390050984.

[50] Uwe Rau and Hans-Werner Schock, 'Cu(In,Ga)Se$_2$ solar cells'. In Mary D. Archer and Robert Hill (editors), 'Clean Energy from Photovoltaics', chap. 7, pp. 277–345 (Imperial College Press, 2001). ISBN 978-1-60119-771-9.

[51] Ingrid L. Repins, Miguel A. Contreras, Brian Egaas, Clay DeHart, John Scharf, Craig L. Perkins, Bobby To, and Rommel Noufi (2008). '19.9 %-efficient ZnO/CdS/CuInGaSe$_2$ Solar Cell with 81.2 % Fill Factor'. *Progress in Photovoltaics: Research and Applications* **16**, pp. 235–239. doi:10.1002/pip.822.

[52] Angus Rockett (2005). 'The effect of Na in polycrystalline and epitaxial single-crystal CuIn$_{1-x}$Ga$_x$Se$_2$'. *Thin Solid Films* **480–481**, pp. 2–7. doi:10.1016/j.tsf.2004.11.038. EMRS 2004.

[53] Stephen Rossnagel, 'Sputtering and Sputter Deposition'. In Krishna Seshan (editor), 'Handbook of Thin Film Deposition Processes and Techniques', chap. 8 (William Andrew Publishing, 2002). ISBN 0-8155-1442-5.

[54] Jens Schöldström, Uwe Zimmermann, and Marika Edoff (2010). 'Dynamic radiative properties of the Cu(In,Ga)Se$_2$ layer during the co-evaporation process'. *Progress in Photovoltaics: Research and Applications* **18** (5), pp. 321–327. doi:10.1002/pip.931.

[55] Dieter Schmid, Martin Ruckh, F. Grunwald, and Hans-Werner Schock (1993). 'Chalcopyrite/defect chalcopyrite heterojunctions on the basis of CuInSe$_2$'. *Journal of Applied Physics* **73**, pp. 2902–2909. doi:10.1063/1.353020.

[56] William N. Shafarman and Lars Stolt, 'Cu(In,Ga)Se$_2$ Solar Cells'. In Antonio Luque and Steven Hegedus (editors), 'Handbook of Photovoltaic Science and Engineering', chap. 13, pp. 567–616 (John Wiley & Sons Inc., 2003). ISBN 0-471-49196-9. URL http://knovel.com/web/portal/browse/display?_EXT_KNOVEL_DISPLAY_bookid=1081&VerticalID=0.

[57] Collaboration: Authors and editors of the volumes III/17E-17F-41C, 'Copper selenides (Cu$_2$Se, Cu$_{2-x}$Se) electronic and transport properties'. In O. Madelung, U. Rössler, and M. Schulz (editors), 'The Landolt–Börnstein Database – Group III: Condensed Matter', vol. 41C of *III* (SpringerMaterials). doi:10.1007/10681727_76.

[58] William D. Sproul, David J. Christie, and Dan C. Carter (2005). 'Control of reactive sputtering processes'. *Thin Solid Films* **491** (1–2), pp. 1–17. doi:10.1016/j.tsf.2005.05.022.

[59] John A. Thornton (1978). 'Magnetron sputtering: basic physics and application to cylindrical magnetrons'. *Journal of Vacuum Science and Technology* **15** (2), pp. 171–177. doi:10.1116/1.569448.

[60] John R. Tuttle, Miguel Contreras, Andrew L. Tennant, David S. Albin, and Rommel Noufi, 'High efficiency thin-film Cu(In,Ga)Se$_2$-based photovoltaic devices: progress towards a universal approach to absorber fabrication'. In '23rd IEEE Photovoltaic Specialists Conference', pp. 415–421 (1993). doi:10.1109/PVSC.1993.347146.

[61] Various authors (2010). 'Key World Energy Statistics'. Tech. rep., International Energy Agency. URL http://www.iea.org/textbase/nppdf/free/2010/key_stats_2010.pdf.

[62] Monica Veszelei, Kent E. Andersson, Carl-Gustaf Ribbing, Kenneth Järrendahl, and Hans Arwin (1994). 'Optical constants and Drude analysis of sputtered zirconium nitride films'. *Applied Optics* **33** (10), p. 1993. doi:10.1364/AO.33.001993.

[63] Erik Wallin, Tobias Jarmar, Ulf Malm, Marika Edoff, and Lars Stolt (2011). 'Influence of the average Se–to–metal overpressure during co-evaporation of Cu(In$_x$Ga$_{1-x}$)Se$_2$'. *Thin Solid Films* doi:10.1016/j.tsf.2010.12.182. In Press.

[64] Henry Windischmann (1992). 'Intrinsic stress in sputter-deposited thin films'. *Critical Reviews in Solid State and Materials Sciences* **17** (6), pp. 547–596. doi:10.1080/10408439208244586.

Acta Universitatis Upsaliensis

Digital Comprehensive Summaries of Uppsala Dissertations from the Faculty of Science and Technology 830

Editor: The Dean of the Faculty of Science and Technology

A doctoral dissertation from the Faculty of Science and Technology, Uppsala University, is usually a summary of a number of papers. A few copies of the complete dissertation are kept at major Swedish research libraries, while the summary alone is distributed internationally through the series Digital Comprehensive Summaries of Uppsala Dissertations from the Faculty of Science and Technology. (Prior to January, 2005, the series was published under the title "Comprehensive Summaries of Uppsala Dissertations from the Faculty of Science and Technology".)